The Role of Low-Level Convergence and Latent Heating in a Simulation of Observed Squall Line Formation

BRUCE B. ROSS

Geophysical Fluid Dynamics Laboratory/NOAA, Princeton University, Princeton, NJ 08542

(Manuscript received 13 February 1986, in final form 25 March 1987)

ABSTRACT

The effects of mesoscale forcing and diabatic heating on the development of convective systems have been investigated using a simplified numerical model to simulate the squall line and the convective system preceding it that occurred over Texas and Oklahoma on 10–11 April 1979. A simulation run without including latent heat showed both systems to be initiated and maintained by convergence produced by larger-scale forcing. The first cloud system formed downwind of the convergence zone that was produced by the confluence of airstreams along a dryline. A cloud front approaching from the west then merged with this dryline, destroying its horizontal gradients through diffusive effects and replacing it with a frontal convergence line that was aligned with the low-level flow. This new configuration was then favorable for the formation of the squall line that developed in the simulation.

When latent heat was included, the continuous cloud in the first convective system broke down into isolated cells which moved downstream from the convergence zone. In the non–latent heat case, the primary mechanism for providing moisture to this cloud was vertical diffusion from the moist surface layer. When latent heat was added, vertical advection within cell updrafts provided a more efficient means to supply moisture to the convective system.

In the simulated squall line, latent heat release produced a deeper cloud system while intensifying and maintaining the low-level convergence. However, unlike the earlier system, the squall line did not break into convective cells when latent heat was included in the simulation.

1. Introduction

The issue of whether low-level convergence exists in the prestorm environment prior to the development of many mesoscale convective systems has importance not only for our understanding of how these systems first develop but also for the potential predictability of such systems by meso-alpha-scale numerical models. The Preliminary Program Design (UCAR, 1984) for the proposed STORM-CENTRAL Experiment cites the determination of whether such convergence precedes storm development as one of the primary research objectives relating to the preconvective environment. A number of observational studies (Fankhauser, 1974; Ogura, 1975; Ogura and Chen, 1977; Koch and McCarthy, 1982) have found evidence to indicate mesoscale lifting to be present up to several hours prior to the first development of convective activity. For such cases in which convergence is an identifiable precursor, the prediction of the resulting convection will be considerably easier. In fact, one can expect deterministic forecasts of the timing and location of convection to require that the triggering mechanism initiating this convection either be resolvable by the model or be able to be effectively represented by the model's subgrid-scale parameterizations.

The extent to which preexisting low-level convergence is important to the development of a given system will be highly case dependent. When it is present, however, one would expect it to play a major role in determining the structure of the convective system that results. In particular, if the lifting zone has a predominantly linear form such as occurs in a surface cold front, one might expect that the resulting convective system would take the form of a squall line. In the case studied here, however, we will find that the direction, relative to the convergence line, of winds in the middle troposphere as well as near the surface may also play a role in determining whether the resulting convection forms an organized line structure or breaks down into isolated cells.

The extent to which latent heat release influences the subsequent development of the storm is also important in determining how much the external forcing will affect further storm development once free convection has occurred. If the atmosphere is conditionally stable, as is the case for most winter storms, the only way to produce and maintain precipitation is through externally forced lifting, usually caused by baroclinic instability. On the other hand, for conditionally unstable cases, such as those typical of the springtime storm environment, the convective system will become self-sustaining once free convection is achieved as long as the moisture supply to the system can be maintained.

When strong large-scale convergence is present, however, this external forcing may continue to influence the storm's development in competition with these diabatic processes.

In analyzing observed storm systems, it may be difficult to separate the contributions to the storm's development from these two effects. A crude but potentially viable way to do this would be to assume stationarity of the prestorm lifting and to attribute any additional parcel lifting to diabatic effects. On the other hand, the process of identifying the influence of latent heat release is quite straightforward in the context of a numerical simulation of a mesoscale convective system, amounting only to the modeler's choice of the value of the heat of condensation to be used.

The importance of latent heat release in producing mesoscale circulations within subsynoptic systems has been demonstrated in several meso-alpha-scale studies of springtime situations involving intense convective activity (Chang et al., 1982; Anthes et al., 1982; Benjamin, 1983). In the case of meso-gamma cloud model studies, however, "turning off" latent heating would usually be quite uninteresting, since such models typically rely upon diabatic effects to maintain the convection once the system has been initially perturbed. A middle range exists between these two extremes, namely that of the meso-beta simulation, for which diabatic effects and external forcing may have similar importance in the formation of a convective system. In fact, Fritsch and Maddox (1981) have used a meso-beta simulation to demonstrate the possible effect of latent heating in organizing a mesoscale convective system, but external forcing was not included in their idealized study. Ideally, a model would resolve the structure of the storm system while at the same time maintaining a realistic representation of the subsynoptic forcing which initiates and may help to maintain it.

In the present study, we will attempt to do this by simulating the development of an observed convective system using a relatively simple meso-beta-scale numerical model. The case to be studied is that of 10–11 April 1979, the first observing day of the SESAME Experiment. The convective outbreak which occurred during this period over Texas and Oklahoma represents one of the most intensively studied events in the history of mesoscale meteorology. (See Barnes, 1985, for a comprehensive bibliography.) The advantage of this case, in addition to the fact that several intense and structurally different convective systems developed during the period, is the availability of upper-air data at 3-h intervals with an average network spacing of roughly 250 km. This dataset, with its high temporal resolution, is needed to provide the lateral boundary conditions which will force the simulation.

A number of mesoscale numerical modeling studies have been carried out for the 10–11 April case. Ross (1986) has identified at least ten different simulations or forecasts of this period. These represent results from seven different numerical models employing several different types of data sources. Most of these studies tend to concentrate on the formation of the convectively unstable environment which preceded the first convective outbreak that developed prior to 0000 UTC 11 April. The squall line which occurred several hours after this time over central Texas received little attention and generally seems to have been poorly simulated by these models. However, Kuo and Anthes (1984) show precipitation maps which indicate the presence of a convective system over northern Texas, apparently representing the squall line in a somewhat diffuse form. Also, Kalb (1985) shows an increase in relative humidity at 700 mb suggestive of the squall line. Both of these are meso-beta-scale simulations in which the upwind boundaries are relatively close to the region where the squall line developed. Out of all of the meso-alpha studies, only the forecast of Orlanski et al. (1984), using First GARP Global Experiment (FGGE) data in their host spectral model, produced a distinct line-type precipitation pattern oriented from southwest to northeast over Texas. From these results, it appears that the cold front that produced the convergence which was ultimately responsible for the squall line formation was overly weak in most of these simulations; evidently the close proximity of prescribed upwind boundaries in the meso-beta studies as well as the more intense winds that were apparently present in the meso-alpha forecast of Orlanski et al. improved the squall line representation. Regarding the boundary proximity, although the nearness of lateral boundaries will usually tend to increase the local noise level due to model adjustment, the imposition of intense low-level winds near the squall line may also tend to intensify convergence where the confluent air streams intersect.

The numerical simulations presented here will not include all of the physical processes which have been incorporated in many other model studies. Rather, we will attempt to simulate the convective development using a model in which some potentially important features, such as terrain and detailed boundary-layer physics, are absent. This approach does not conflict with the findings of Carlson et al. (1983) and Benjamin and Carlson (1986) that these effects are important for the development of the potentially unstable prestorm environment. Rather, we will assume here that their influence has already produced features important to the preconvective environment such as the capping inversion and the differing air masses that force the simulation through their specification on the model inflow boundary conditions.

Section 2 provides a description of the development of the observed convective systems. Section 3 includes a brief description of the numerical model and the preparation of the dataset used for the initial and boundary conditions. Also, a discussion is given of how the meso-beta model produces and enhances mesoscale

features from the coarser observational data. Section 4 presents results from the numerical simulations. Cloud features from the basic simulation are shown and compared with corresponding satellite imagery. Then a comparison is made of the effects of low-level mesoscale convergence and latent heating on development of the convective systems by comparing simulations without and with latent heating included. An analysis is also presented of the evolution of the simulated surface front and its effect on the dryline structure as the two lines merge. A discussion of results is given in section 5, including a trajectory analysis of air parcels flowing into each storm system. Finally, conclusions are presented in section 6.

2. Observed Conditions

The synoptic conditions associated with the 10–11 April case have been described by several authors (see e.g., Moore and Fuelberg, 1981) and will only be reviewed briefly here. Primary emphasis in this paper will be concerned with development of the squall line over central Texas during the period from 2300 UTC 10 April to 0600 UTC 11 April and a comparison between this and the convective system that developed prior to it over northern Texas and southwestern Oklahoma.

At 1200 UTC 10 April, a deepening surface low was located over Colorado with a surface front extending south into New Mexico. A stationary front was positioned in an east–west orientation near the Gulf Coast. Also, a southerly low-level jet was located over eastern Texas and Oklahoma. During the next 12 h, the cold front to the west moved into the Texas Panhandle, while the front along the Gulf moved north as a warm front to a location at 0000 UTC along the Texas–Oklahoma border (Fig. 1a). A jet streak moved from New Mexico into west Texas around the upper-level trough located to the west (Fig. 1b). The low-level jet, apparently acting in response to this jet streak passage (Carlson et al., 1980), intensified during this period. An inversion also formed over the lower terrain of eastern Texas as a result of differential advection of dry air from the Mexican plateau passing over moist low-level air moving northward from the Gulf (Carlson et al., 1983). A dryline over western Texas marked the western edge of the moist southerly flow. This dryline moved east to meet the southern edge of the capping inversion by 0000 UTC 11 April (Fig. 1a).

Convection first developed after 1800 UTC (1200 CST) as a line of thunderstorms (oriented from southeast to northwest) just south of the Texas Panhandle. By 2100 UTC (1500 CST), the line had moved east to the vicinity of the Red River Valley. Behind this convective line, a more isolated, intense storm developed to the west-southwest of Witchita Falls, Texas, before 2200 UTC. This storm moved to the east-northeast toward the Red River Valley (see Fig. 2a and 2b) producing the most damaging tornadoes of the SESAME I period from 2300 UTC (1700 CST) to 0400 UTC 11 April (2200 CST) (Alberty et al., 1979). During this period, satellite photographs showed the upwind (southwest) portion of the storm cloud shield moving to the northeast into Oklahoma (Fig. 2a–2c).

While this system was developing, a narrow line of convection formed over west-central Texas just prior

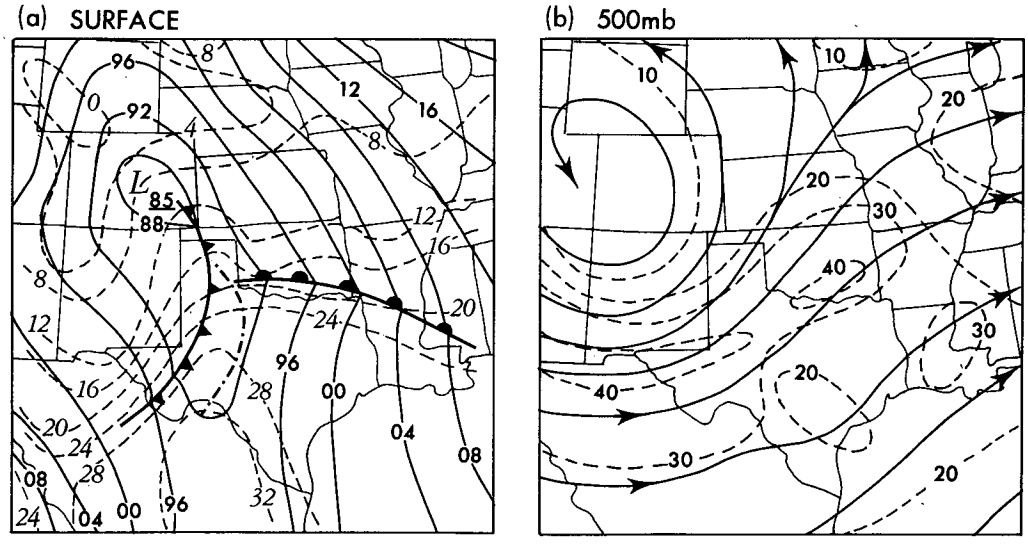

FIG. 1. Synoptic charts of 0000 UTC 11 April 1979. (a) Surface conditions, including sea level pressure (solid contours, in units of mb with only last two digits shown) and surface isotherms (dashed contours, in units of deg. C). Dryline is indicated by the dash–dot line. (b) The 500-mb winds (dashed contours indicate isotachs, in units of m s^{-1}). Figure adapted from Figs. 17 and 18 of Anthes et al. (1982).

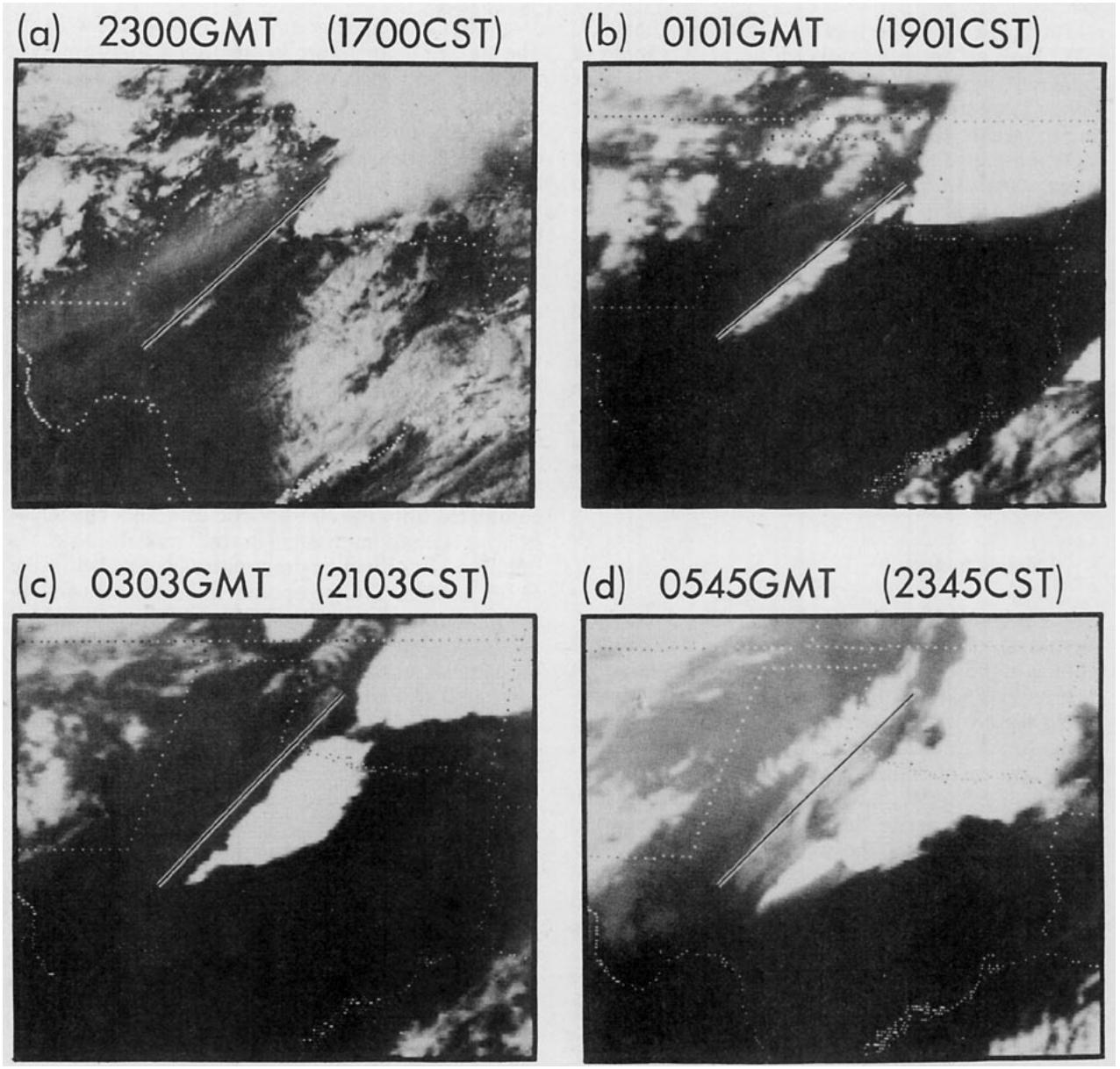

FIG. 2. Satellite photographs showing (a) visible and (b–d) infrared imagery. A reference line has been added at the same location in each frame to indicate the position of the initial development of the cloud system.

to the 2300 UTC (1700 CST) satellite photograph. Figure 2a shows this initial development as a thin band of clouds between Midland and San Angelo, Texas, just east of the southern end of the reference line shown in the figure. (The reference line, which is used in this and subsequent figures, is the approximate western border of the squall line clouds in the satellite photographs.)

As shown by the first two frames of the satellite photographs in Fig. 2, convection initially developed from southwest to northeast along a line that corresponded to the orientation of the dryline over west-central Texas. Comparison of the cloud development with the reference line indicates a slight southwestward growth and an extensive northeastward development between 2300 UTC 10 April and 0101 UTC 11 April. However, during this period, there was essentially no motion perpendicular to the reference line. Convective intensity was also quite weak initially, as indicated by the fact that the Midland, Texas radar, located 110 km to the west, did not observe any reflectivity signature from the line until approximately 0130 UTC. Thereafter, the storm developed rapidly, producing the first severe weather report of damaging hail northwest of San An-

gelo at 0216 UTC (Alberty et al., 1979). Also after 0130 UTC, the line began to move eastward at a speed of roughly 10 m s^{-1}. This behavior suggests that the earlier clouds along the line shown in frames 2a and 2b were due to weaker forcing which produced shallow convection oriented along the dryline. The later explosive growth observed from radar data (not shown) resulted from the arrival of a stronger forcing mechanism, apparently the eastward-moving cold front, that produced much more intense low-level convergence.

By 0303 UTC (Fig. 2c), the deep convection occurring parallel to the reference line produced a cloud shield associated with the earlier convective system over central Oklahoma. At 0545 UTC (Fig. 2d), the major axis of the squall line continued to move eastward with its cloud shield merging with the clouds of the system to the northeast. The southwestern portion of the cloud system lagged behind somewhat, possibly due to localized effects of orography.

3. Modeling approach

The present study will employ a rather simple numerical model in an effort to simulate the essential features of the squall line and the environment in which it developed without including many of the complicating features which were present at the time of its formation. The effect of the larger-scale forcing upon the development of this system is provided by an analysis of the SESAME rawinsonde observations which were used to prescribe the conditions on the upwind inflow boundaries of the model domain. However, these observed data are still relatively coarse compared to the meso-beta-scale structure of the squall line and the convergence zone which produced it. It is therefore essential for the mesoscale model to enhance the larger-scale features imposed at the model boundaries in order to produce the required mesoscale structure as will be demonstrated in subsection 3c. This model enhancement of the mesoscale features will also be discussed.

a. Brief description of the model

The mesoscale model used here is quite similar to that described by Ross and Orlanski (1982). The model uses an anelastic, hydrostatic formulation of the equations of motion on a Cartesian coordinate system with the height z as vertical coordinate. The horizontal grid resolution is 20 km and the vertical grid spacing is nearly 1000 m, with the model lid located at 15 km; the finite-difference grid staggering is type C under the Arakawa convention (Arakawa, 1972). The limited-area domain has open lateral boundary conditions which use the local normal velocity to determine whether inflow or outflow conditions exist. Surface winds are controlled by a simple bulk aerodynamic drag with the drag coefficient, C_D, equal to 0.25×10^{-3}.[1] The surface temperature is prescribed from observations in order to provide some effect of surface heating. The vertical gradient of water vapor is set to zero at the surface, implying no water vapor flux across the lower boundary. Fourth-order diffusion is used in the horizontal to reduce high wavenumber noise. The vertical diffusion coefficient employed in the model depends primarily upon the local Richardson number, as was described in Ross and Orlanski (1982).

The model uses an explicit formulation of moist convection with a latent heating term included in the energy equation. The equation system contains a prognostic equation for cloudwater. Rainwater is not predicted prognostically but rather is generated by autoconversion when cloudwater exceeds a threshold value, specifically when the cloudwater per unit volume exceeds 1.5 g m^{-3}; this rainwater is then removed immediately from the system and added to the total accumulated from the atmospheric column. (The inclusion of falling rainwater in the model, which is important in providing evaporative cooling below the cloud, is difficult to incorporate in a consistent way in the present model with its 20-km grid increment and will be postponed to a later study.) Finally, because of the smaller horizontal grid size used in this model compared to earlier simulations (e.g., Orlanski and Ross, 1984; Orlanski et al., 1985), saturation is assumed here to occur at 100% relative humidity rather than 95% as was used in these earlier simulations.

A major simplification of the model lies in the absence of orographic effects in the equation formulation. The result of this is to eliminate the mean effect of the terrain slope from northwest to southeast in the simulation. If the goal of this study were to simulate the development of the different air masses which interact in the storm region, the lack of orography as well as the simplified treatment of the surface heating used here would be a serious limitation of the model (Benjamin and Carlson, 1986). However, because these air masses are already formed by the time they reach the domain (inflow) boundaries, their characteristics are believed to be represented adequately by the observed boundary conditions without requiring direct terrain effects within the model.

The extent of the model domain as well as the height of the actual terrain are shown in Fig. 3. The primary region of interest in this study will be confined to the southwestern portion of this domain, consisting of north-central Texas and southern Oklahoma. This region is strongly controlled by the inflow boundaries to the south and west. The extension of the model domain to the north and east, as shown in the figure, is done

[1] This relatively small value has been chosen because the large vertical grid spacing would produce an overly deep layer of large shear if larger values of C_D were used.

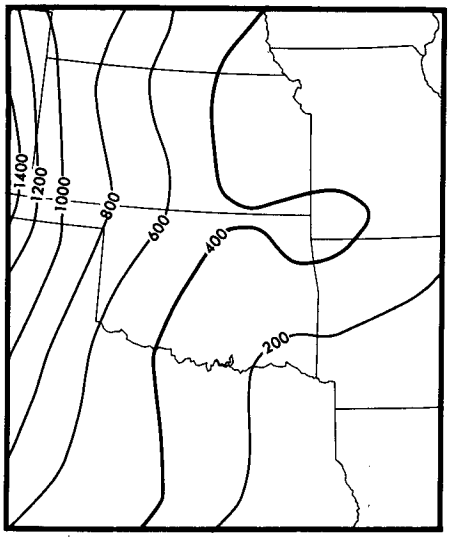

FIG. 3. Map of model domain with contours indicating height above sea level, in meters, of actual terrain. Heavier dark contour corresponds to constant height of model surface.

to reduce the influence of disturbances along these downstream boundaries.

The height of the model's lower boundary was chosen as 400 m, which corresponds to the heavier contour in the figure. This contour roughly bisects the domain and represents the approximate surface height at which the squall line reached maturity. The low-level winds approaching the squall line from the Mexican plateau generally followed the contours of the terrain, while the winds from the west boundary tended to move more downslope after the cold front entered the domain and thus were more influenced by the absence of terrain in the model. The assumption made here is that these steeper downslope effects were of only secondary importance for the dynamics of the flow within the model domain. In fact, for a wind speed of 20 m s^{-1} following the surface, these slopes (less than or of order 1:400) over west Texas upwind of the region of interest would produce a vertical velocity at the surface of only 5 cm s^{-1}, which will be found to be quite small compared to vertical velocities produced above the convergence zone, even without latent heating effects.

b. *Preparation of initial and boundary data*

The dataset which was used for initial and boundary conditions in the numerical simulations was kindly provided to the author by Dayton Vincent and Thomas Carney of Purdue University. The procedures which they employed in the preparation of this analysis of the SESAME rawinsonde and surface observations have been described by Vincent et al. (1981) and Vincent and Carney (1982). Their approach involved an objective analysis of the surface data and the rawinsonde soundings at 25-mb increments onto a 1° latitude–longitude grid over the SESAME domain. The data were then vertically smoothed to pressure surfaces at 50-mb increments.

These gridded data, which were provided at 3-h intervals for the period 1200 UTC 10 April to 1200 UTC 11 April, were then interpolated to the present model grid using the techniques described by Ross and Orlanski (1982). Because the model surface is located at a height of 400 m above sea level, it was necessary to provide bogus data at model grid points located below the physical surface. As Fig. 3 shows, the region requiring such a procedure was primarily confined to the northwestern part of the domain. The vertical grid spacing in the model is roughly 1 km, and the grid staggering requires a half-grid increment displacement of thermodynamic variables and horizontal winds above the model surface. Therefore the only points requiring special treatment of horizontal winds and water vapor are located where the earth's surface is above a height of 900 m. However, potential temperature must be extended down to the actual model surface at 400 m above sea level for use in the temperature boundary conditions; Fig. 3 shows this region to be restricted to an area immediately adjacent to the west boundary. The extrapolation method is straightforward and assumes a well-mixed layer. Horizontal winds are assumed to have zero vertical shear. Potential temperature is extrapolated adiabatically to the model surface, while water vapor is assumed to have a constant mixing ratio.

c. *Model enhancement of mesoscale features*

The SESAME dataset provides a considerable improvement in both spatial and temporal resolution over that of the standard operational rawinsonde network. With an average station spacing of roughly 250 km and a nominal time interval of 3 h between balloon releases, these data offer nearly a twofold improvement in station separation and a fourfold increase in the number of soundings per day. This resolution is still not sufficient to resolve many of the mesoscale features of interest here, including the squall line and the mesoscale convergence which precedes it. We must therefore rely upon the considerably higher resolution of the model and its associated dynamics to enhance the larger-scale forcing imposed at the lateral boundaries and therefore to produce the necessary meso-beta features of interest here.

Although the present model was initialized at 1200 UTC 10 April, sensitivity studies performed by Orlanski et al. (1984) suggest that cases such as the present solution, with its relatively small domain, will be dominated by lateral boundary conditions rather than initial conditions at the time when the squall line is developing. Using a meso-alpha model for a limited-area domain of roughly 5000 by 3000 km, Orlanski et al. demonstrated that solutions with the same lateral boundary conditions but with different initial conditions converged to very similar solutions after only 1 day of integration. Similar results that indicate the po-

tentially dominant influence of lateral boundary conditions in limited-area simulations have also been reported by Anthes et al. (1985). It is reasonable to expect that the time required for boundary conditions to dominate should be on the order of the transit time of an air parcel through the model domain. In the present case, this time is approximately 10 h, suggesting that lateral boundary forcing will dominate the current solution prior to 0000 UTC 11 April, which is well before the time of squall line development.

Figures 4 and 5 show comparisons, respectively, of horizontal and vertical fields between observations and the model simulation at 0300 UTC 11 April. In each figure, the left frames are taken from observations and the right frames from the model simulation with latent heat effects excluded. The region shown in Fig. 4 is roughly the southeastern two-thirds of the complete model domain and represents the primary region of interest in this paper.

At low levels (the lower two frames of Fig. 4), the model wind field indicates a considerable intensification of the wind gradient, compared to the analyzed winds, along a line in the western half of the domain. This increased gradient is created in the model as the colder air from the west encounters the warmer air from the south and southwest. In the observational analysis, the cyclonic turning of the air entering from the west occurs more gradually over a distance of several hundred kilometers, which roughly corresponds to the separation of the rawinsonde stations, as one might expect. The low-level temperature fields also reflect this convergence of airstreams. In the observations, a broad tongue of warm air enters the domain from the southwest between the cold front to the northwest and the moist air to the east; however, in the model, this warm air is squeezed between these two airstreams with stronger temperature gradients separating the different regions.

In contrast to the lower levels, the winds in the middle troposphere (the upper row of Fig. 4) show little difference between observations and simulation. The only significant differences appear in the model results

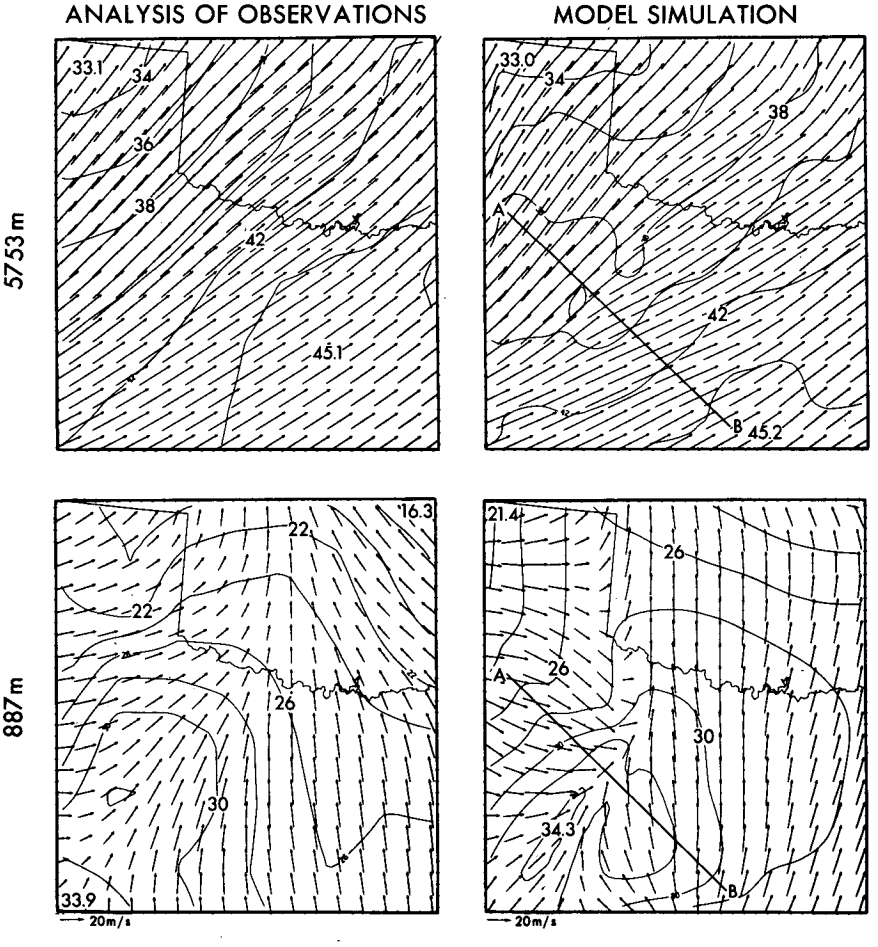

FIG. 4. Comparison of winds (vectors) and potential temperature (contours, in deg. C) for two heights, 887 and 5753 m, at 0300 UTC between simulation without latent heat and analysis of observations. Line segment, AB, indicates position of vertical cross section used in Fig. 5.

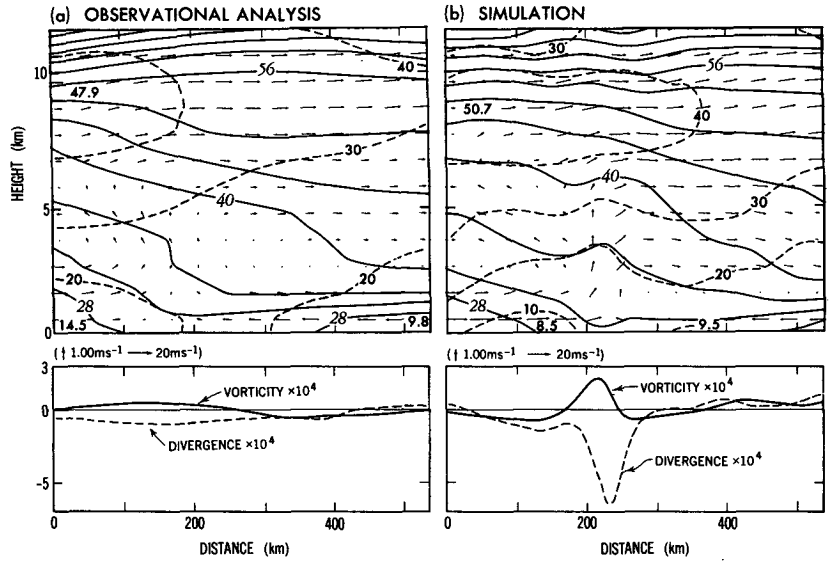

FIG. 5. Comparison between observations and simulation without latent heat, both at 0300 UTC, for vertical cross section, AB, indicated in Fig. 4, showing potential temperature (solid contours, in deg. C), winds in the plane (vectors), and wind speed normal to plane (dashed contours, in m s^{-1}). Lower plots show corresponding distributions of divergence and vorticity, in s^{-1}, at 887 m height.

as an eastward deflection of the wind; this deflection indicates a divergent flow acting at this level in response to the line of convergence at the 887-m level. The potential temperature field in the simulation indicates the adiabatic cooling associated with this line of upward motion. The mesoscale features appearing in the simulation occur not only as smaller-scale effects such as a more intense convergence zone but also as increased gravity wave structure which has been largely filtered by the observational analysis. Some of these waves are excited by adjustment in the model fields that occur near the left inflow boundary. Temperatures along the western and southern inflow boundaries in the simulation have been prescribed from the observations; hence, while the interior temperature exhibits these waves, the net temperature gradient spanning this region between the western and southern boundaries must be determined by these prescribed boundary conditions.

Figure 5 shows a comparison between observations and model results at the same time but in the vertical cross section defined by the line segment AB which is roughly perpendicular to the convergence line evident in Fig. 4. This figure shows potential temperature (solid contours), wind component perpendicular to the cross section (dashed contours), and wind vectors within the plane. Below each contour map is a plot of relative vertical vorticity and horizontal divergence at 487 m above the model surface, which is the first interior grid point. The structure of the surface cold front is evident on the left side of the frames with the jet stream in each frame exhibiting a similar value of maximum cross-plane wind; however, the strong jet stream wind extends further to the right in the simulation.

As was evident in Fig. 4, the major differences between the simulation and the observations occur in the lower levels below 5 km. This disparity is caused by the substantial increase of both convergence and vorticity near the surface cold front in the simulation. The plots of these fields show this intensification quite clearly. The observed fields exhibit a broad region (250 km wide) of weak vorticity and convergence with a corresponding layer of weak upward motion extending up to 7 km. On the other hand, the model produces a narrow band of intense convergence and vorticity having a width of roughly 100 km.[2] As in the observations, the associated layer of upward motion extends to a height of 7 km; however, because this upward motion in the model is much more intense (over 80 cm s^{-1}), the contours of both potential temperature and cross-plane winds show considerable vertical displacement. This structure is similar to that shown in other frontal simulations involving intense vertical motion (Ross and Orlanski, 1978; Orlanski and Ross, 1984). The dramatically increased low-level convergence in the model is due to the strong low-level wind component within the cross-sectional plane to the left of the updraft

[2] The vorticity and divergence in the present frontal system have a similar structure to that shown by Ross and Orlanski (1984, see their Figs. 3 and 4), in which the maximum convergence is located at the zero vorticity node ahead of the region of positive vorticity. The larger convergence compared to vorticity in this case probably reflects the more intense mesoscale forcing from the boundary.

zone (compare wind vectors in Fig. 5). Reference to Fig. 4 indicates that this larger wind component directed along AB is caused by a clockwise rotation of the model winds from their direction in the observations with the total wind speed being comparable to observations.

Another feature of this case is the strong restraining inversion which is evident below 2 km on the right side of each frame in Fig. 5. While the stability of this layer remains fairly intense from the right border to the surface front in the observations, it is weakened considerably in the simulation, apparently due to the frontal lifting as well as the relatively coarse vertical resolution in the model.

4. Development of the squall line

The simulation of the squall line, which will be seen to be quite realistic within the limitations of the model's resolution and simplified physics, provides a better understanding of the development of this system. It will be most instructive to compare the formation of this convective line with that of the more cellular convection associated with the first convective outbreak which preceded it. In order to distinguish the dynamic forcing mechanisms which initiated these convective systems from the diabatic effects which later intensified them, we will compare solutions without and with latent heating included in the numerical model. However, before considering these differences, we will first look at the cloud structure of the full simulation with diabatic effects included and compare it with observations.

a. Cloud features of the full simulation

The basic simulation with latent heating included was run, as in the non–latent heat case, for the period from 1200 UTC 10 April, when no convection was present in the observations, to 0600 UTC 11 April, when the first convective outbreak had moved well into Oklahoma and the Texas squall line was well developed. In this simulation, the first convection occurred as an isolated system in the Texas Panhandle adjacent to the western border at around 1900 UTC 10 April and moved to the northeast. A second region of clouds, involving a more continuous generation of convective elements, then developed in the region somewhat to the south of this, beginning around 2300 UTC. The first convective system, indicated by the letter "A" in Fig. 6, developed at 1900 UTC; its initiation time was close to that of the first observed convection, but its location was too far south into Texas. The second system, indicated by the letter "B", occurred several hours too late in its development compared to the corresponding observed storms which moved into the Red River Valley around 2300 UTC.

The time period, 0100 to 0500 UTC, of the cloud fields shown in Fig. 6 corresponds to the interval in which the squall line develops in the simulation. The algorithm used to show the structure of the cloud patterns in this figure is the same as that employed by Orlanski and Polinsky (1984), namely that stippling intensity is used to indicate the total amount of cloud-water in the column. At 0100 UTC, a line of convection is predicted to occur along the southwest border of Oklahoma, while an older, more isolated system has moved into southcentral Kansas. Comparison of this field with the satellite image of Fig. 2b shows general similarity between the simulated and observed cloud shields within the field shown in Fig. 2[3] but with the simulated clouds displaced to the west of observations. This displacement seemed to be caused by a delay in the development of the simulated storm, possibly because of the slow development of the cold front in the model as discussed in section 4c. However, both the simulated and observed storms developed in the Texas Panhandle west of the Red River Valley and then moved eastward as a system (although individual convective "cells" moved to the northeast). A weaker cloud system also developed near the center of the eastern border, apparently due to upgliding motion associated with the warm front which extended east from Oklahoma.

At 0300 UTC the primary convective system in the simulation had moved to the northeast, although new convective elements developed over southern Oklahoma. Also the first indications of squall line development are evident over northern Texas. While this convection began over 1 h later than in the observed case, it occurred at approximately the same position, relative to the reference line, as the observed squall line (Fig. 2c). By 0400 UTC, this line convection extended to the southwest, parallel to the reference line. This tendency to develop new convection on the upwind end of the line is characteristic of "back-building" squall lines, as referred to by Bluestein and Jain (1985). As in the observed case, the cloud shield extended northeastward but had not reached the northern system in the simulation by this time, probably because of the delay in its initial development. However, the distance of the convective line from the reference line and the shape of the cloud shield are quite similar to that of the observed system.

Clouds associated with the warm front formed a denser solid line normal to the eastern boundary by 0500 UTC. Neither these clouds nor those that had formed in the southeast corner were convectively active. Both of these features may have been affected by the artificially elevated terrain to the southeast and by interaction with the eastern boundary.

[3] The general absence of clouds downwind over Missouri in the simulation is not supported by observations, possibly because the excessively elevated terrain in this area does not permit sufficient moisture from the Gulf to reach this region in the model.

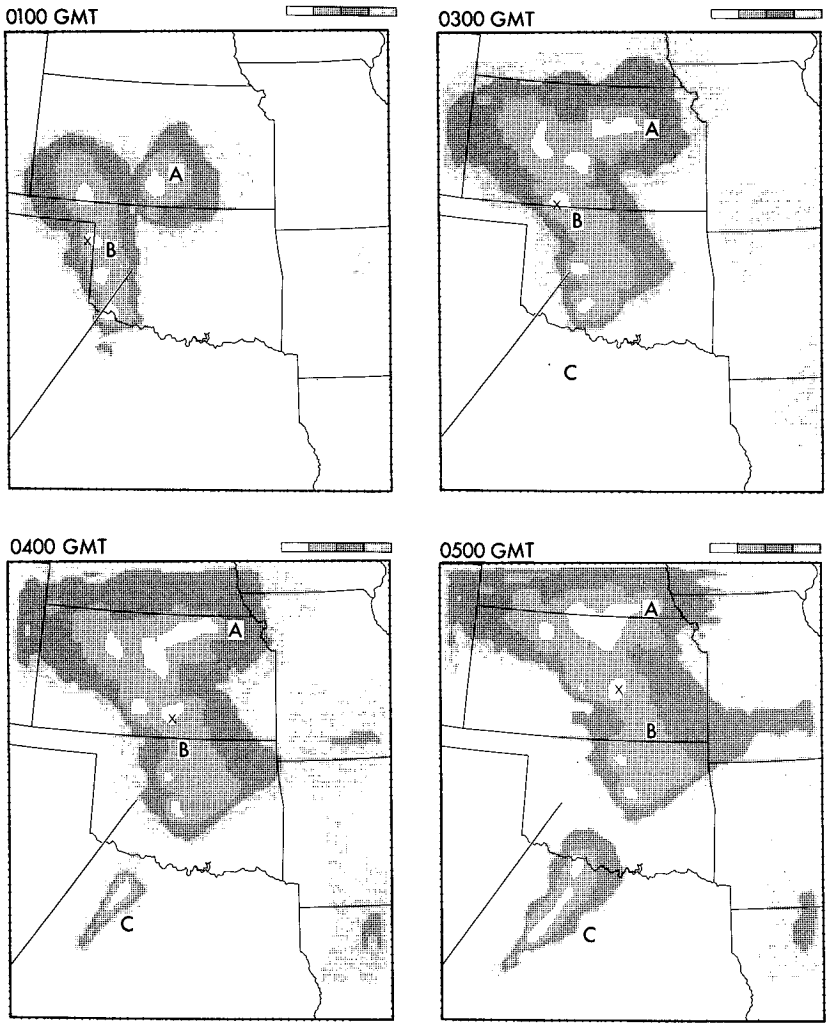

FIG. 6. Plots of vertically integrated cloudwater amounts at four different times from simulation with latent heat included. The letter X shows position of maximum total cloudwater amount. Letters A, B, and C designate different convective systems. Reference line is at the same position as that in Fig. 2.

b. Effect of low-level convergence without latent heating

The cloud structure from the simulation without latent heating (Fig. 7) and the corresponding structure when latent heating is included (Fig. 6) show a number of similarities. Each of the major convective systems occurring over Texas, Oklahoma, and Kansas in the latter figure is also identifiable in the former. The total column-integrated cloudwater amount in Fig. 7 is considerably less than in Fig. 6, reflecting the shallower cloud depth in the case without latent heat. This reduced cloud penetration also causes a reduction in the downstream extent of the cloud shield or anvil in Fig. 7 because of the reduced wind speed occurring at these lower heights. However, the similar location of the dense cloud regions in each figure suggests that the mechanism creating these source regions in the case with latent heating is also present in the solution without latent heating.

Figure 8 shows the correspondence between the cloudwater field (stippled area) at 1860 m height and the wind and moisture fields at 887 m, which are shown for the same times as in Fig. 7. A region of maximum convergence (solid contours) occurs upstream of each cloud zone. This convergence is also aligned with the dryline interface, which is indicated in the figure by the line of large gradient of water vapor mixing ratio (shown primarily by the dashed contours of 6 and 9 gm kg^{-1}). In fact, the moist, cooler air east of this line flows almost due north and provides a low-level barrier to the more westerly flow from the west. Trajectory analyses (presented in section 5) of the origin of air parcels within the southern portion of each cloud for the times shown indicate that inflow from low levels

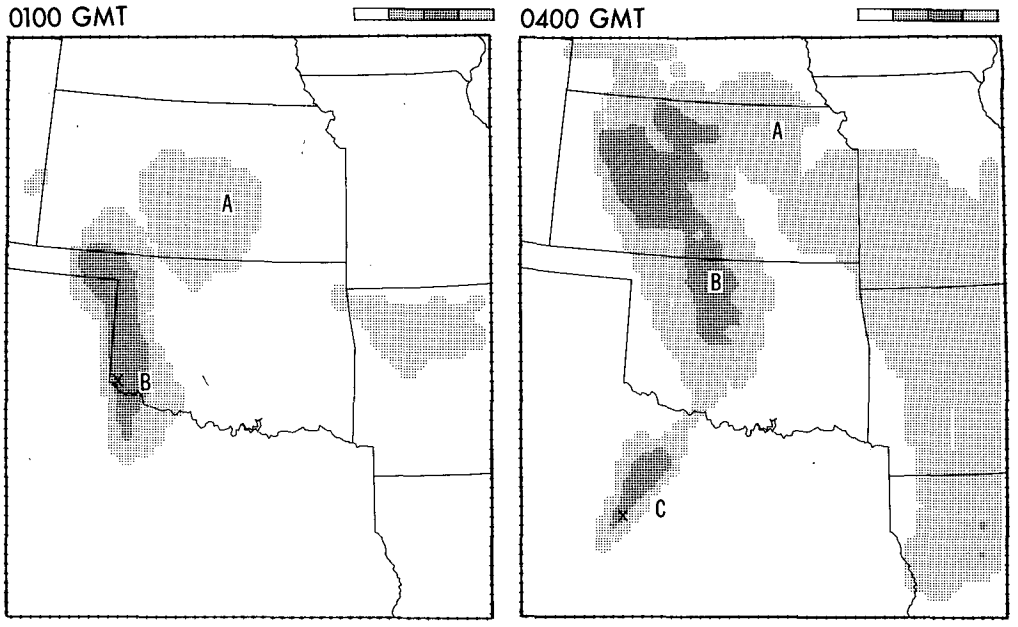

FIG. 7. As in Fig. 6 except taken from case without latent heat.

occurs along a path from the southwest, defined approximately by the indicated line segments AB and CD. These line segments are parallel to each other and reflect the persistent flow direction of the weakly stratified warm air mass originating over the Mexican plateau. Finally, note that the inflow direction for AB is oriented at an angle to the major axes of both the cloud and the convergence zone at 0100 UTC; however, at 0400 UTC, the corresponding inflow for CD is in alignment with the cloud and the major axis of the convergence zone. This change in orientation seems to explain the structure of the resulting cloud system, particularly the "dog-leg" turn at the Texas–Oklahoma border which is evident in the cloud pattern at 0400 in Figs. 7 and 8.

Vertical cross sections (Fig. 9) taken along the lines AB and CD for the corresponding times indicate more clearly the different way in which the low-level convergence produces clouds for the two different times. A comparison of the horizontal wind speeds within the plane (the horizontal component of the vectors) and perpendicular to the plane (dashed contours) shows the flow below 4 km and ahead of the zone of upward motion to remain roughly within the plane in both

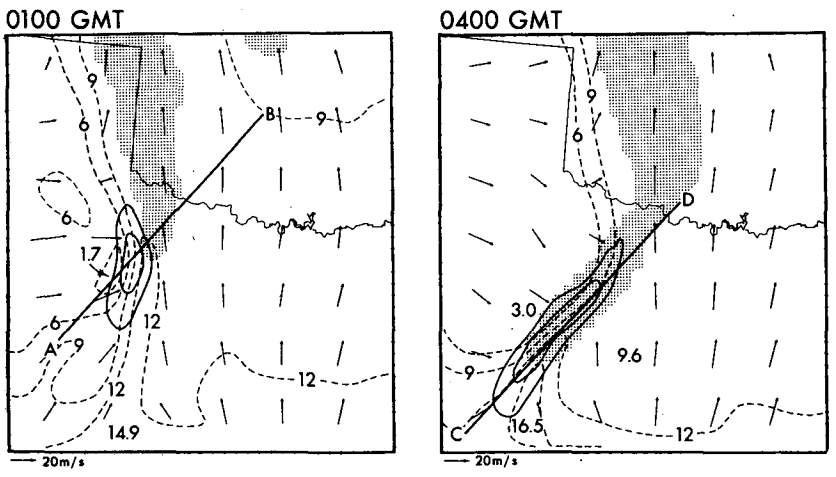

FIG. 8. Composite plots from simulation without latent heat, showing cloudwater at 1860 m height (stippling); convergence (solid contours, in intervals of 25×10^{-5} s^{-1}); water vapor mixing ratio (dashed contours, in units of g kg^{-1}); and winds (vectors), all at 887 m height. Line segments, AB and CD, indicate positions of vertical cross sections, at designated times, in Figs. 9 and 15.

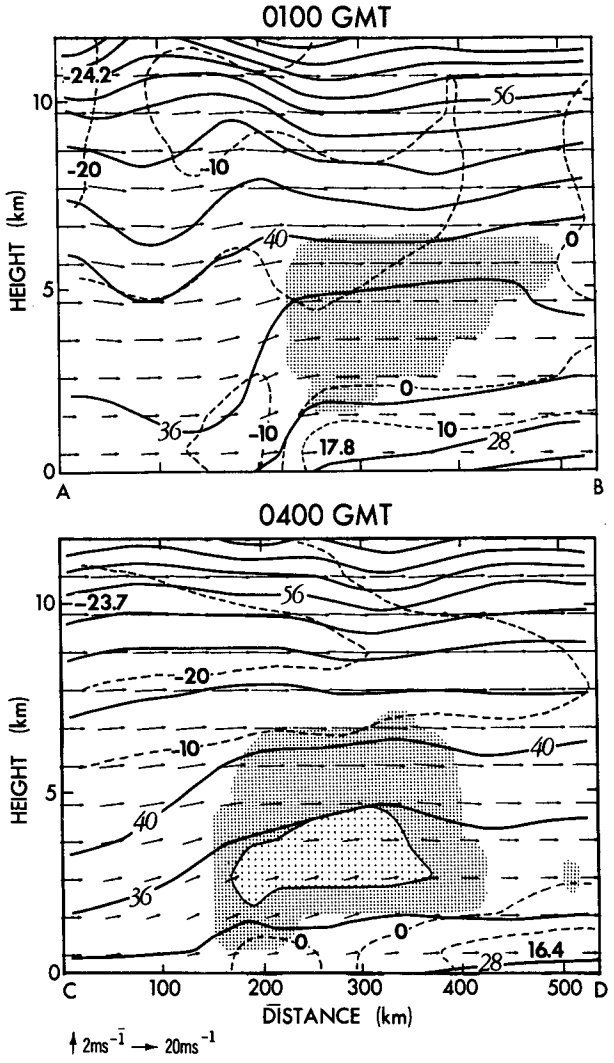

FIG. 9. Maps for vertical cross sections, AB and CD, indicated in Fig. 8, showing cloudwater (stippled regions, where lighter inner stippling indicates mixing ratios greater than 2 g kg^{-1}), potential temperature (solid contours, in units of deg. C), winds in the plane (vectors), and wind speed normal to the plane (dashed contours, in units of m s^{-1}).

cases. At 0100 UTC, the upward motion is quite abrupt as the low-level flow encounters sloping isentropes (solid contours) and strong cross-plane winds to the northeast. Because the updraft is narrow, the cloud zone itself is also narrow at the base with a shallow anvil extending downstream at higher levels. Note that the stratification of the warm air mass below 5 km is weak ahead of the convergence zone, thus permitting deeper penetration of air parcels when they encounter the low-level convergence.

At 0400 UTC, the zone of upward motion is shown in Fig. 9 to be much wider, thereby producing a broader low-level cloud zone within the cross section. At the same time, both the isentropes and cross-plane winds vary more gradually in the horizontal due to the closer alignment of the cross section with the interface between air masses. Finally note that the magnitude of the maximum vertical speed at 0400 UTC is comparable (the maximum vertical velocity is around 70 cm s^{-1}) to that at 0100 UTC; however, it now extends over a region of several hundred kilometers compared with an extent of less than a hundred kilometers at the earlier time.

The forcing mechanism producing the cloudwater zone in the simulation develops through an interaction of different air masses within the solution. These air masses are identifiable by their low-level temperature and wind direction. Figure 10 summarizes the evolution of these fields in the solution without latent heat for the period during which the squall line developed. The warm air mass moving into the domain from the southwest is indicated by shading inside the 33°C contour of potential temperature (thin contours). The moist air mass to the east can be identified by southerly wind flags (plotted at every fifth model grid point). Finally the cool, dry air behind the cold front appears to the north of the warm air mass. The initial structure of the temperature contours and wind flags in the latter region prior to 0300 UTC is not consistent with that of a typical surface cold front. This apparently is due to the artificial response of the model to the boundary conditions associated with the entry of the frontal system; these features also reflect to some extent the fact that data at this level were extrapolated down from the actual earth's surface, which is roughly 800 m above the model surface in the most northwestern corner of the domain in Fig. 10. However, from 0300 UTC on, the frontal structure becomes more realistic at a time when it is becoming more important to the development of the convergence zone.

Figure 10 shows clearly how the convergence zone rotates clockwise from a north–south orientation at 0000 UTC to a southwest-to-northeast alignment at 0300 UTC. This is accompanied by a similar rotation of the eastern border of the warm air mass. At the same time, the northeastern border moves southeastward as the cold front moves into the domain. As the surface front overtakes the dryline, the region of potential temperature greater than 33°C is reduced and finally eliminated as the front and dryline merge. Note also that the peak convergence increases to a maximum of 80×10^{-5} s^{-1} at 0300 UTC as the lines first merge and then decreases after the low-level region of warm air has collapsed. This maximum apparently occurs because the frontogenetic convergence reinforces the previous convergence zone that was produced by upgliding motion along the air mass boundary, i.e., the dryline.

c. Influence of the cold front

The evolution of the surface cold front and its influence on the flow field as the front merges with the dry-

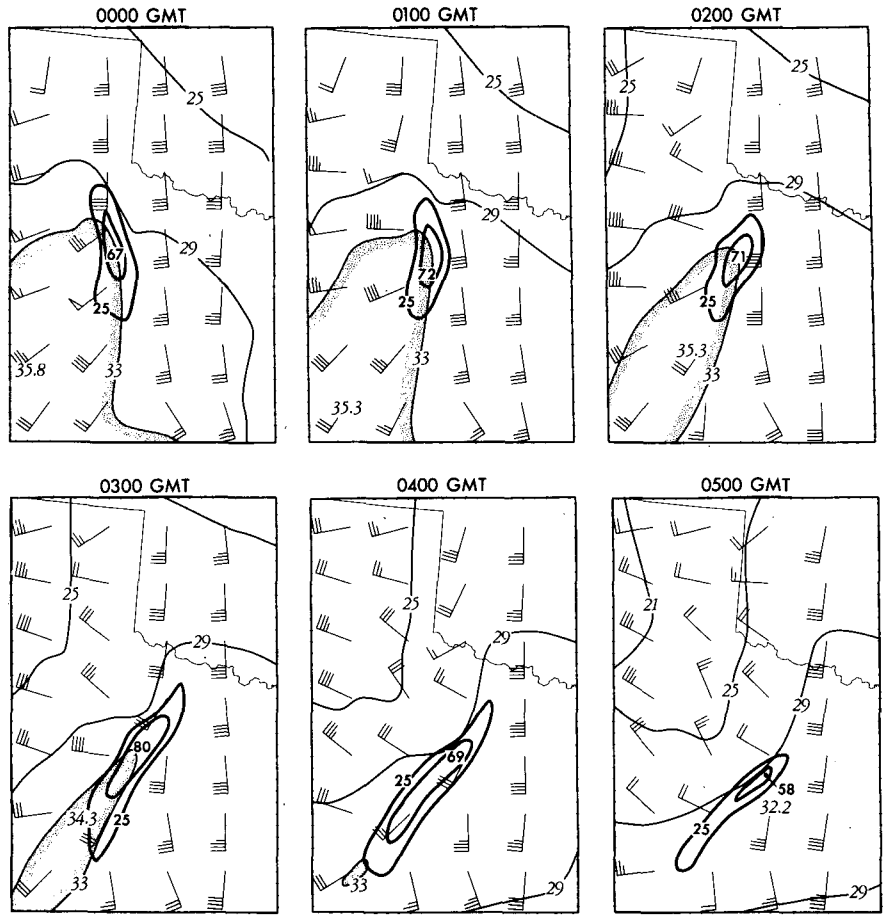

FIG. 10. Comparison of convergence (heavy contours, in units of 10^{-5} s^{-1}), potential temperature (light contours, in units of deg. C), and winds (flags, using standard meteorological convention) for simulation without latent heat at 487 m above the surface.

line are important aspects of the simulation. (This merger of the front and dryline has been studied by Koch, 1984, in the case of a developing squall line.) The magnitude of the horizontal temperature gradient near the surface provides a valuable indicator of the position of both the cold front and the dryline. Figure 11 shows contours of this gradient magnitude field for the same height, time period, and domain extent as shown in Fig. 10 in order to facilitate comparison with that figure.

At 0000 and 0100 UTC, the north–south gradient line, indicating the position of the dryline, roughly matches the location of the 33° isotherm in Fig. 10. The cold front approaching from the northwest, as suggested by the isotherms in Fig. 10 at 0000 UTC and 0100 UTC, is still ill defined, as discussed earlier. However, at 0200 UTC, a secondary gradient maximum appears in Fig. 11 on the north end of the dryline. This feature, as well as the local maximum to the southwest, indicates the development of a more coherent surface front, which is indicated at 0200 UTC and thereafter by a dashed line in the figure.

During the period of frontal approach to the dryline, the gradient maximum in the dryline is seen to weaken and move southward, suggesting a deterioration of the dryline temperature gradient to the north. This process continues at 0300 UTC with the front intensifying as the dryline gradient weakens. The striking feature of nearly parallel gradient lines in Fig. 11 at 0300 UTC is consistent with the squeezing of the warm surface air between the cold front and the dryline as shown in Fig. 10. The subsequent eastward motion of the front at 0400 UTC and 0500 UTC causes the remaining dryline gradient to be pushed well to the south as the frontal gradient intensifies to dominate the flow field. Reference to Fig. 10 shows the front actually extending to the western boundary but with a progressively weaker gradient to match the weaker temperature gradient imposed by the inflow conditions.

The evaluation of the frontogenetic/frontolytic processes associated with a cold front, as first studied by Miller (1948), is a valuable way to define the dynamic mechanisms associated with the intensification of a front. Koch (1984) has performed an analysis of the

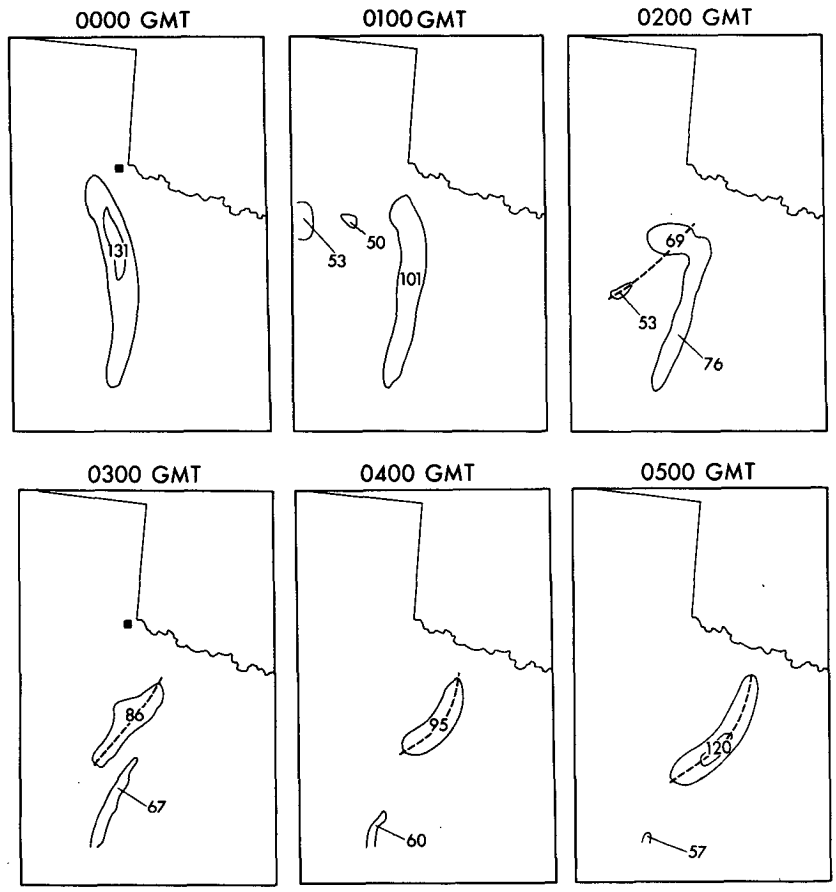

FIG. 11. Plots of the magnitude of the horizontal potential temperature gradient (in units of 10^{-6} °C m^{-1}) at a height of 887 m from the simulation without latent heat. The contour interval is 50×10^{-6} °C m^{-1}. The dashed line, shown from 0200 to 0500 UTC, is the analyzed position of the surface cold front. The box symbols indicate the position of the sounding site referenced in Fig. 13.

frontogenetic function, which is the substantial derivative of the horizontal gradient, in order to explain the development of a squall line that was observed to form along a surface front. He concluded from this analysis that a transverse frontal circulation, enhanced by contrasts in the surface sensible heating, produced the observed squall line development.

In the present case, we will evaluate the relevant individual frontogenetic terms that are responsible for the weakening of the dryline and the intensification of the cold front. The procedure used here is similar to that followed by Orlanski et al. (1985), who computed the terms for 15 successive model time steps (representing a total of nearly 6 model minutes) and then averaged so as to filter high frequency noise. The complete form of the frontogenetic equation is given schematically as follows:

$$\frac{d}{dt}|\nabla_H\theta| = \text{convergence} + \text{deformation} + \text{twisting} + \text{diffusion} + \text{latent heating}$$

where

$$\text{convergence} \equiv -\frac{1}{2|\nabla_H\theta|}(\theta_x^2+\theta_y^2)(U_x+V_y)$$

$$\text{deformation} \equiv -\frac{1}{2|\nabla_H\theta|}[(\theta_x^2-\theta_y^2)(U_x-V_y) + \theta_x\theta_y(U_y+V_x)]$$

$$\text{twisting} \equiv -\frac{\theta_z}{|\nabla_H\theta|}(\theta_x W_x+\theta_y W_y)$$

$$\text{diffusion} \equiv \frac{1}{|\nabla_H\theta|}[\nabla_H\circ\nabla F]$$

$$\text{latent heating} \equiv \frac{1}{|\nabla_H\theta|}[\nabla_H\theta\cdot\nabla H].$$

Figure 12 shows the three dominant terms, convergence, deformation, and diffusion, for the same level (487 m above the model surface) as in Fig. 11 and for times before, during, and after the merging of the cold

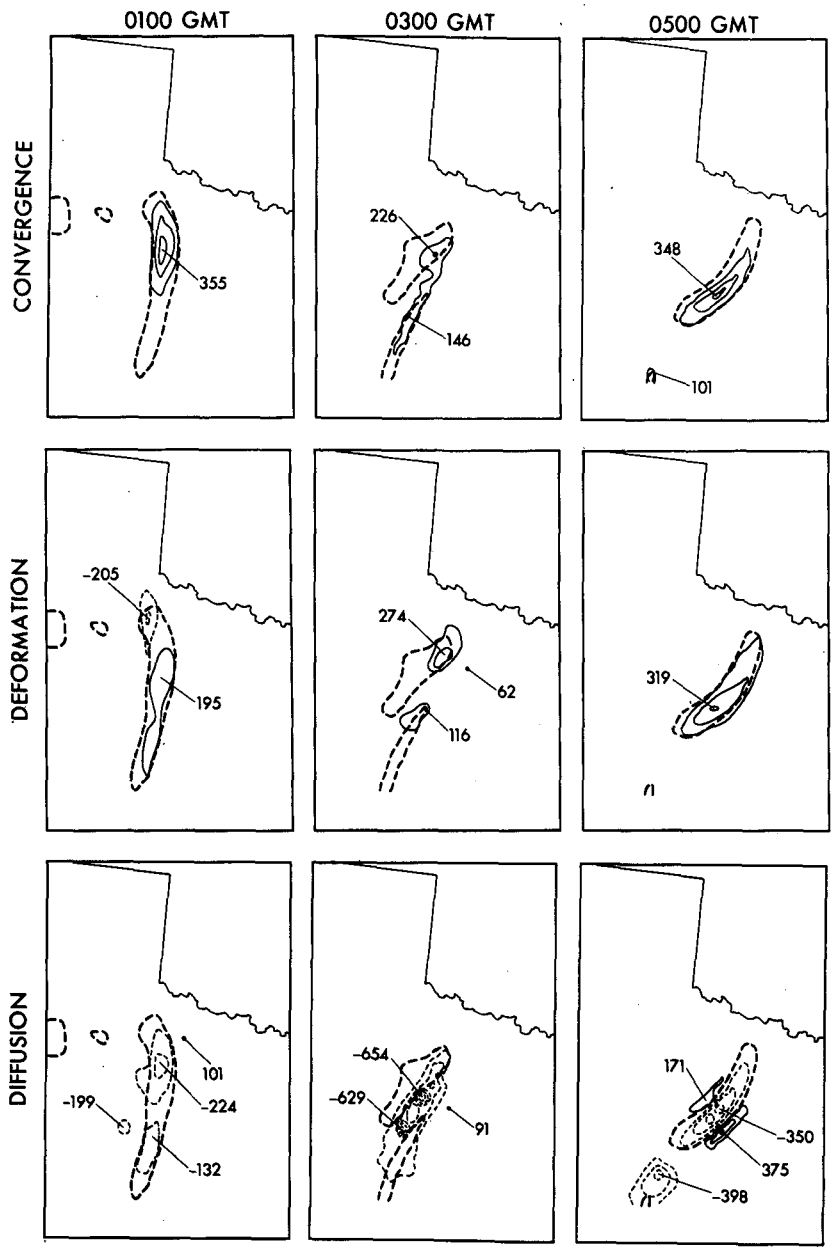

FIG. 12. Composite map of the important frontogenesis terms as calculated from the non-latent heat simulation at a height of 487 m above the surface for times prior to, during, and following the merging of the front and dryline. Frontogenetic regions have solid contours, while frontolytic areas have dotted contours. Labels are in units of 10^{-10} °C m^{-1} s^{-1}; the contour interval is 100 units. Contours of temperature gradient, as in Fig. 11, are reproduced as dashed lines for reference.

front and dryline. Regarding the other two terms, the latent heating term is zero in this case, while the twisting term is quite small at this height, which is the first grid point above the surface. Frontogenesis is indicated in the figure by solid contours and frontolysis by dotted contours. The corresponding temperature gradient fields are reproduced as heavy dashed contours for the purpose of reference.

The initial fields at 0100 show the form of the terms for the dryline structure. Convergence is the dominant positive term and occurs on the north end of the dryline where the convergence shown in Fig. 10 is maximum. The negative diffusion somewhat counteracts this convergence and balances the positive deformation to the south. Deformation is negative on the extreme northwest end of the dryline. This apparently has the effect

of weakening the gradient there and contributes to the clockwise rotation of the dryline evident in Fig. 11.

The most significant aspect of the front–dryline merger period of 0300 UTC is the dominance of diffusion effects. This is evident in the very large negative diffusion term lying between the front and dryline gradients in the figure. This frontolytic term produces the rapid decay of the dryline adjacent to the front. This result from the model simulation suggests that turbulent mixing played a dominant role in the breakdown of the dryline in this case as the cold front merged with it. At the same time, even though the convergence itself is shown in Fig. 10 to reach a maximum value at this time, the convergence term in Fig. 12 is considerably weaker than at 0100 UTC. This is explainable by the fact that the temperature gradient across the convergence line is now much weaker as the air masses merge.

By 0500 UTC, the terms associated with the cold front exhibit a more typical form characteristic of an isolated cold front (although the lengthwise extent of the apparent front is quite short). Both convergence and deformation are strongly frontogenetic, while diffusion is frontolytic in character, except for small positive regions adjacent to the frontal line. The diffusive region at the front–dryline intersection has moved south as the extension of the front, with too small a gradient to be contoured in Fig. 11, moves to the south.

Finally, in view of the importance of the surface cold front to the evolution of the dryline and the development of the squall line, it is worthwhile to evaluate the movement and intensity of the simulated front by comparing it with observations. A comparison of the frontal position and characteristics at 0300 UTC were made using Figs. 4 and 5 for the non–latent heat simulation and the analysis of observations; this showed the analyzed and simulated positions to be similar, although the scales of the analyzed front are inevitably quite broad.

A potentially more severe evaluation of the frontal structure involves a comparison of "soundings" obtained from the model solution with actual observed soundings. An attempt to compare model results with surface observations was inconclusive, primarily because of poor surface station coverage in key areas over Texas. This comparison has the advantage that individual observed soundings do not involve the strong smoothing that is inherent in objective analyses; on the other hand, the raw soundings are contaminated with small-scale noise that would normally be eliminated by an analysis procedure. The sounding site chosen for this comparison is located at Childress, Texas, indicated in Fig. 11 by solid boxes at 0000 and 0300 UTC proximal to the southwest corner of Oklahoma. This site was chosen for two reasons. First, the data from the three soundings for the period are fairly complete and do not show any direct effects of local convection. Also, the site is well away from the model borders and is situated where it can provide an indication of the frontal movement during the period. Figure 13 shows a comparison of winds and potential temperature taken from the SESAME observations and the model output, both of which have been vertically interpolated to 25-mb pressure levels. For the sake of simplicity, the model soundings are vertical and instantaneous for the times shown, with no attempt made to simulate balloon rise rate or drift.

The comparison shows a number of similarities as well as some revealing differences. The winds above 700 mb are quite similar in both direction and speed, in agreement with Figs. 4 and 5, although there is some tendency for the observed winds to be somewhat larger. The major difference occurs in the wind direction below 800 mb, particularly for the earliest time (2312 UTC in the observations, 0000 UTC in the simulation). Similarities are also evident but less striking between the observed and model temperature fields in the middle and upper troposphere. The major difference in temperature also appears to occur in the lower levels around the first sounding time. Some of these discrepancies, such as that related to the strong cooling in the observations near the surface, are attributable to the simplicity of the model's treatment of surface conditions and its coarse resolution of the boundary layer. However, the primary cause appears to be due to a delay in the passage of the surface front through this site as compared to the observations. In fact, when wind "soundings" were taken hourly in the model rather than on the 3-h interval shown in the figure, the 0100 sounding was found to exhibit a low-level wind direction very similar to that shown in the first observed sounding (with a release time of 2312 UTC). Hence there appears to be a delay of nearly 2 h in the effective frontal passage at Childress in the model compared to observations. This delay may not be a simple shift in the movement of the front but rather may reflect a slower development of the front at this position due to inflow boundary influences. In any event, this delay would appear to explain the slow formation of the squall line compared to observations, as was found in subsection 4a from the comparison of model cloud patterns with satellite imagery.

d. Latent heating effects

With the inclusion of latent heating in the model solution, a considerable increase in the vertical motion can be expected in the potentially unstable regions when air parcels are lifted to their level of free convection. The vertical displacement of over 1000 m produced by the convergence zone, as indicated in the cross sections of Fig. 9, should be sufficient to achieve free convection if the air parcels advected from the southwest ahead of the zone contain sufficient moisture. This will be the case for the 0400 UTC case in the non–latent heat case; however, at 0100 UTC, vertical diffusion above the moist layer seems to be re-

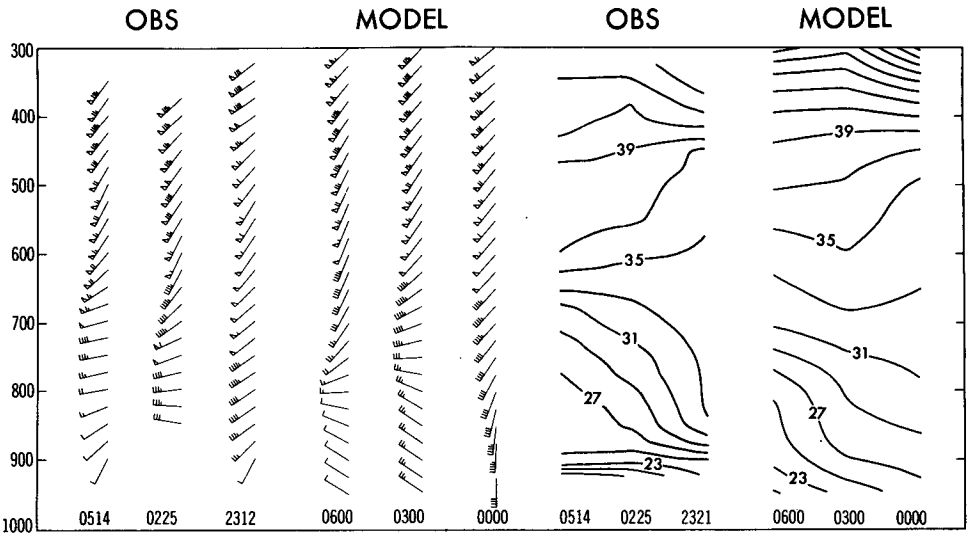

FIG. 13. Comparison of horizontal winds and potential temperature between observed soundings and model-derived "soundings" at Childress, Texas (see Fig. 11 for location) for the three sounding times of interest. See text for details. The horizontal wind barbs use the standard meteorological convention; a northward wind direction is indicated by a vertically pointing wind flag. The contour interval for potential temperature is 2°C.

quired in order to produce saturation and free convection because of the dryness of the air in low levels upwind of the convergence zone. The trajectory analysis presented in section 5 will further clarify this point.

Figure 14 shows the horizontal convergence field at 487 m above the surface from the solution with latent heating at 1-h intervals for the period from 0000 to 0500 UTC 11 April. This figure should be compared with the convergence contours in Fig. 10. Such a comparison shows the southwestern, upwind portion of each convergence zone in Fig. 10 to be virtually identical with that in Fig. 14. In fact, the maximum convergence for the latent heat case within each large lifting zone prior to 0400 is quite close to the corresponding peak in the non-latent heat case. However, Fig. 14 shows the northern end of the convergence zone to be distorted when latent heat release is included in the model. As parcels move from the southwest into the zone, their lifting initially has little effect on the convergence, until saturation is achieved and a net positive buoyancy is then produced by diabatic effects. Thereafter, however, vertical motion is intensified as the convective instability is released.

In the present model, latent heat release is included explicitly in the model's energy equation. Therefore, when a condition of free convection develops within the model, a small-scale "cell" develops in the presquall line case with intense vertical motion above and corresponding larger convergence near the surface. Figure 14 shows the creation of several of these cells on the northeast end of the larger-scale lifting zone. As each cell intensifies and penetrates into the middle troposphere, it begins to move to the northeast, driven by the stronger winds higher in the atmosphere. This mechanism explains the behavior of the convergence fields in the figure prior to 0300 UTC with cells being shed from the downwind side of the larger-scale zone as they form and intensify. The subsequent displacement of these cells during the next hour is indicated by the arrows shown in each frame. Note that the intensity of each cell's surface convergence tends to be maximum in the vicinity of the larger-scale convergence zone and then decreases as it moves downstream. If these cells are the meso-beta model's equivalent of isolated supercells, one cannot expect them to be sufficiently well resolved by the 20-km resolution model to have the necessary updraft–downdraft structure required for their maintenance over a period of several hours. However, while their initial development is shown from trajectory analyses (section 5) to have been produced by air parcels from the southeast, they are subsequently fed by the very moist air east of the dryline once their surface convergence intensity increases. As a result, they become separate convective entities, with some similarities to isolated supercells, once they move away from the original meso-beta scale lifting zone.

At 0300 UTC and later, the behavior of the mesoscale convergence changes. Unlike the convergence at earlier times, the lifting zone at 0300 UTC is quite similar to that of the non-latent heat case along its entire length. It thus appears that parcel lifting has not had time to produce significant latent heat effects in this region at this time. However, by 0400 UTC, diabatic effects have caused a major change. On the one hand, Fig. 10 showed the nondiabatic convergence maximum to be decreasing after 0300 UTC, once the

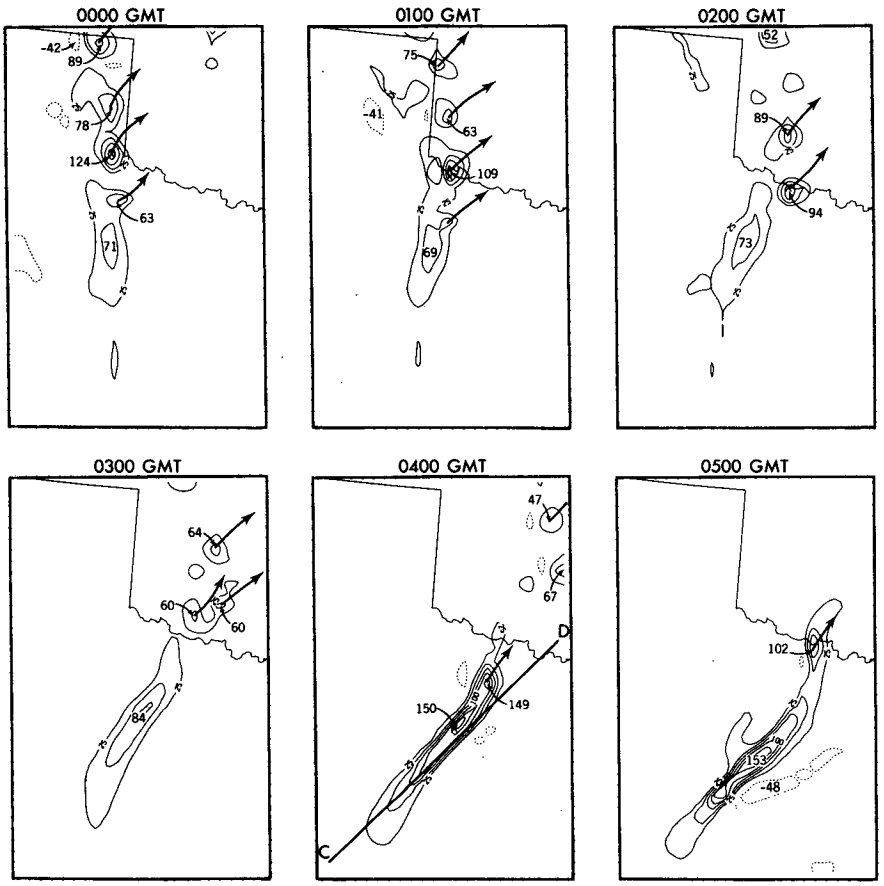

FIG. 14. Comparison of divergence (in units of 10^{-5} s^{-1}) at 887 m height from simulation with latent heat included. Line segment, CD, at 0400 UTC is at same position as in Fig. 8. Arrows extending to the northeast indicate the cells' movement during the next hour.

surface front has merged with the dryline. On the other hand, Fig. 14 shows a near doubling of the convergence maximum between 0300 and 0400 UTC with latent heat included. At the same time, the band remains relatively intact over a distance of 400 km. There is a gradual increase in convergence along the band from zero in the southwest extreme to a maximum of 150 $\times$ 10^{-5} s^{-1} beyond the middle of the line. The downwind end of the band apparently produces a separate cell after 0400 UTC which breaks off and moves downstream as seen in the 0500 frame. However, unlike the earlier convective system, cell formation along much of the squall line tends to be suppressed even though latent heating within the line is quite intense.

Figure 15 shows wind, potential temperature, and cloud fields in the vertical cross section indicated by the line segment CD in the 0400 frame of Fig. 14. This line segment is identical to that used for the nonlatent heat case of Fig. 8. Comparison of Fig. 15 with the 0400 UTC frame of Fig. 9 shows that, upstream of the cloud zone, the potential temperature and wind fields are virtually unchanged by the inclusion of latent heating, as one might expect. However, within the cloud, diabatic warming due to latent heating produces a potential temperature increase of over 9°C. (While this anomaly may be possible for the updraft core of a supercell, it is unrealistically large in the present case considering its horizontal extent in the model.) At the same time, the vertical velocity increases to a maximum of 4.3 m s^{-1} near the rear of the cloud where the temperature increase is largest. This intense lifting also creates adiabatic cooling in the lower levels of the storm where the temperature decreases to nearly 2° below that of the nonlatent heat case. The deep penetration of the cloud causes the winds near 10 km to deflect toward the east as shown by the larger negative maximum of the wind component directed out of the plane in the upper part of the cloud.

The map of total precipitation from the 18-h simulation with latent heat included (Fig. 16) provides a summary of the way in which convection developed within the model. Initially, convection occurred over the northern extreme of the Texas Panhandle with the resulting storm moving off to the north-northeast as a

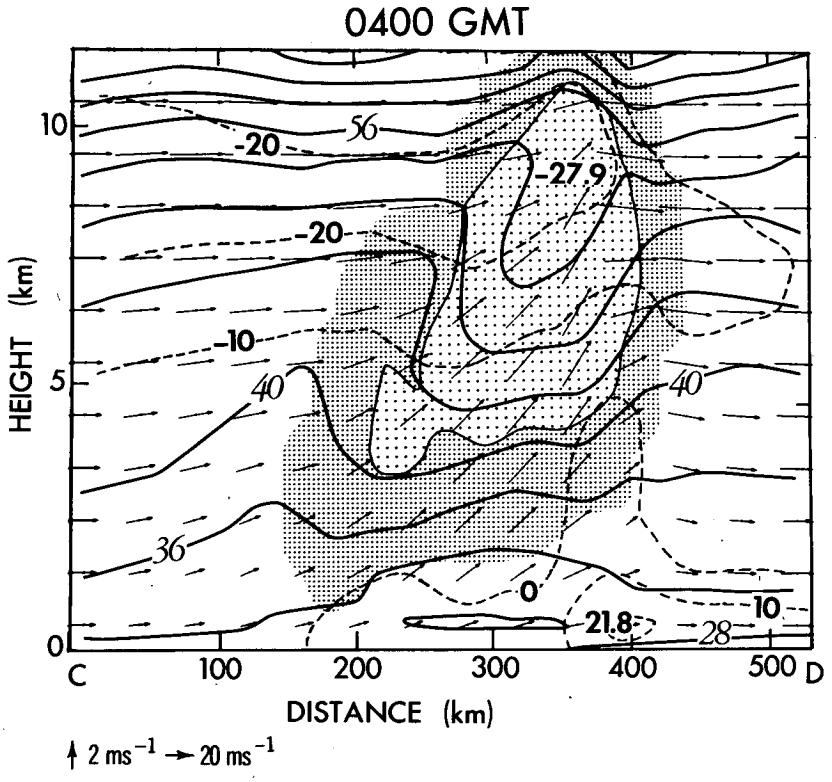

FIG. 15. As in Fig. 9 but taken from run with latent heat included. Cross section corresponds to line segment, CD, shown in Figs. 8 and 14.

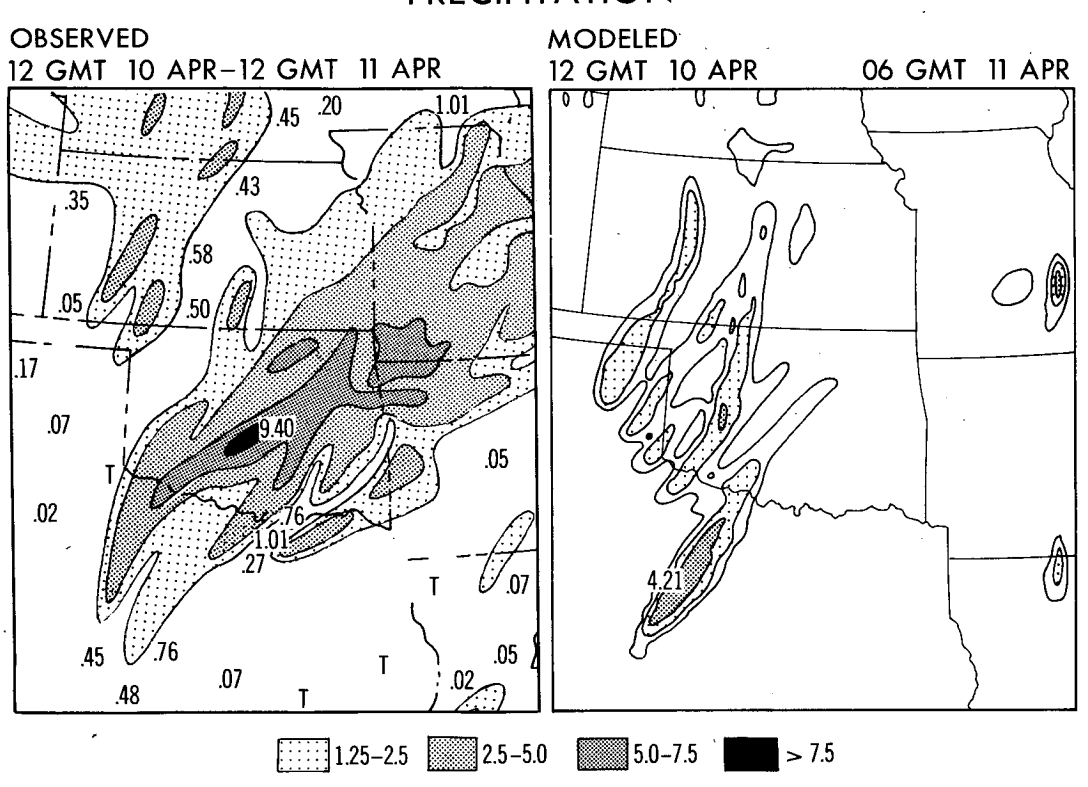

FIG. 16. Comparison between observed 24-h precipitation (left frame) and 18-h model precipitation (right frame). Amounts are given in cm of rainwater. (Analysis of observed precipitation is courtesy of Heavy Precipitation Forecasting Group, National Meteorological Center.)

narrow track of rainfall. Then as the convergence zone moved toward the southeast, new storm cells formed which also moved downwind in a similar direction. Finally the axis of the convergence zone rotated to align with the direction of the previous storm tracks as the front overtook the dryline, and the squall line developed. Because of the increased efficiency for rain production of this system, compared to that of the isolated convective cells, the squall line generated the maximum precipitation of the simulation. Also, the interaction of convection with the eastern boundary produced localized rainfall maxima, which were apparently far enough away to have had no effect on the region where the squall line developed.

An analysis of observed precipitation for the 24-h period from 1200 UTC 10 April to 1200 UTC 11 April is also shown in the figure for comparison with the model results. Warm season precipitation is recognized as one of the most difficult quantities for a numerical model to predict (see, e.g., Fawcett, 1977). In fact, because of the small scale, and intermittent nature of convectively generated precipitation, the analysis of such rainfall is itself subject to considerable uncertainty (Kreitzberg, 1979; Ross, 1986). Even with these difficulties, it is useful to compare observed and predicted rainfall for the present model, since such a comparison provides another way in which to verify the starting location and track of the simulated convective systems. This comparison indicates similar starting location and direction of the early rainfall tracks between observations and simulation. In particular, note the similar orientation of the rainfall lines in southwestern Kansas. The precipitation associated with the modeled squall line is larger than was observed at the location shown. However, it is similar in magnitude to the observed rainfall maximum occurring 100 km to the west, suggesting that this disparity may reflect the delay in the simulated squall line's development as it moved eastward.

The simulation clearly misses the major precipitation amounts occurring downstream over central Oklahoma and into Missouri. Much of this rain seems to have been associated with the first convective system which developed prior to the squall line. This deficiency may be due in part to the artificially elevated terrain used in the present model which will tend to reduce the southerly flow of moisture on the eastern side of the domain. A further cause of the reduced rainfall to the northeast is the tendency, as mentioned earlier, for isolated cells to decay in the model as they move downstream of the large-scale convergence zone. This premature decay seems to be due to the inability of the meso-beta model to portray the meso-gamma scale structure properly, including the gust front caused by evaporative cooling, that is thought to maintain these long-lived supercell systems which produced most of the precipitation in the first convective outbreak. The squall line, however, is more meso-beta-scale in its structure and thus is better represented by the model.

5. Discussion of results

The position of the 0000 UTC convergence on the downwind side of the warm air mass, where the dryline bulges to the northeast, is consistent with the preferred region for severe storm development for a class of springtime severe weather cases in the Oklahoma–Texas region as analyzed by Moller (1979, 1980). Moller (1980) presented an analysis of surface observations from 10 April which showed this case to be quite typical of situations in which severe storms develop northeast of the dryline bulge. In particular, some of the major features common to such cases are a north–south orientation of the thermal ridge to the west, a moist tongue of air east of it, and strong winds in the middle troposphere directed toward the northeast. The latter winds are at an angle to the axes of the thermal ridge and the moist tongue and therefore blow across the dryline interface separating them.

The intensity of the dryline convergence will be determined primarily by the strength of the wind component near the surface directed normal to the line. Danielsen (1974) has suggested that this low-level flow intensifies when stronger winds in the middle troposphere are entrained into the well-mixed boundary layer over the heated terrain to the west. McCarthy and Koch (1982) have concluded that this downward transport mechanism was partly responsible for a similar observed convergence zone that occurred along the dryline prior to the convective outbreak in a case which they analyzed. They also observed a region of blowing dust immediately upwind of the convergence zone in this case; Danielsen suggested that such blowing dust was evidence of the intensification of these boundary-layer winds. Similar indicators were evident in the 10 April case as well, including a swath of blowing dust in the visible satellite imagery at 2300 UTC (Fig. 2a) immediately west of the reference line and surface observations of blowing dust and gusty winds in this same region.

Analysis of the simulation also shows strong low-level winds ahead of the dryline. However, because of the model resolution of the boundary layer, the simplified physics used to represent it and the short distance over which boundary-layer mixing can act upstream of the dryline, it is unlikely that such mixing can cause a major change in the low-level wind profile between the time when air enters the domain and reaches the convergence zone. Rather it is more probable that these boundary-layer effects, if they occurred, acted largely outside of the model domain to form the vertical wind structure which was prescribed on the inflow boundaries.[4] The effect of the model's treatment of the

[4] The technique of constructing bogus fields below the terrain, as was described in section 2a, may also contribute to the more intense winds in the lower layer by its effect on the wind profile prescribed at inflow boundaries. However, this should only be significant at locations along the western boundary where terrain heights exceed 1000 m above sea level (see Fig. 3). Such points are located north of the inflow region affecting the convergence zone.

boundary layer on the formation of the convergence zone has been tested by performing sensitivity tests in which the magnitude of the drag coefficient C_D was increased by factors of 2 and 5 over its control value of 0.25×10^{-3}. Comparison of low-level convergence, wind and temperature structure (not shown) indicates virtually no change in the convergence zone when C_D is doubled. Increasing the coefficient to five times the control produces some changes in the structure of the lifting zone but only a slight weakening of its magnitude. This insensitivity of the convergence to changes in C_D provides further evidence of the dominance of the inflow boundary conditions in determining the structure of the lifting zone.

The effect of low-level convergence and latent heat release on cloud formation can be shown more clearly by means of a trajectory analysis of the developing convective system. This analysis has been done for cases with and without latent heat for two representative times: 0100 UTC, prior to squall line formation, and 0400 UTC, when the squall line was well developed. A predictor–corrector iterative method was used to obtain trajectories from model history data which were saved at time intervals of 7.5 min (20 time steps). Trajectories were integrated backwards in time, starting from points located within the cloud system. In order to compare differences due to diabatic effects between the shallower cloud without latent heat and the deep cloud with latent heat, all trajectories were integrated backwards from a height of 2400 m above the surface.

Figure 17 shows a comparison of three-dimensional clouds and trajectories for the two cases at 0100 UTC, which was nearly 2 h prior to the first appearance of clouds within the simulated squall line. The clouds shown represent regions in which cloudwater exceeds 0.10 gm kg^{-1}. The domain extends up to 6.5 km in the vertical and covers the southwestern two-thirds of the horizontal area shown in Fig. 8. In Fig. 17, the northern boundary is identified by a vertical plane. The dashed contours indicate the approximate positions of the dry line as denoted by the 9 gm kg^{-1} line of water vapor mixing ratio at 887 m height (projected down to the surface). Each parcel trajectory terminates at the same height (2400 m) with the vertical lines denoting parcel positions at 15-minute time intervals.

The cloud systems, both with and without latent heat included, are each located in the same position just east of the dryline. However, the more intense upward motion occurring in the latent heat case produces dramatic differences in the structure of the system. The clouds to the south (toward the right side of the figure) extend deeper into the atmosphere when diabatic effects are included. Also, in contrast to the continuous cloud field shown in the left frame, the cloud with latent heat forms a cellular structure consistent with that produced in the low-level convergence pattern of Fig. 14. These cells tend to merge at middle levels in the northern end of the system. Finally, one should recognize that plotting the 0.10 gm kg^{-1} cloudwater surface alone can be somewhat misleading, since this tends to overemphasize regions of small cloudwater such as that shown by the weak cloud above 5 km evident in the foreground of each frame in Fig. 17. (The increase in cloudwater content when latent heat is included is clearly shown by a comparison at 0400 UTC between Figs. 9 and 15 of the area of light stippling, the region where cloudwater amounts exceed 2 gm kg^{-1}.)

The trajectory paths of parcels entering both clouds are most instructive in indicating how each system is formed and maintained. In the case without latent heat, parcels flow smoothly into the lower levels of the cloud from the warm drier air to the west. By comparing heights of these paths moving back in time, one can conclude that parcel A was still being lifted by the con-

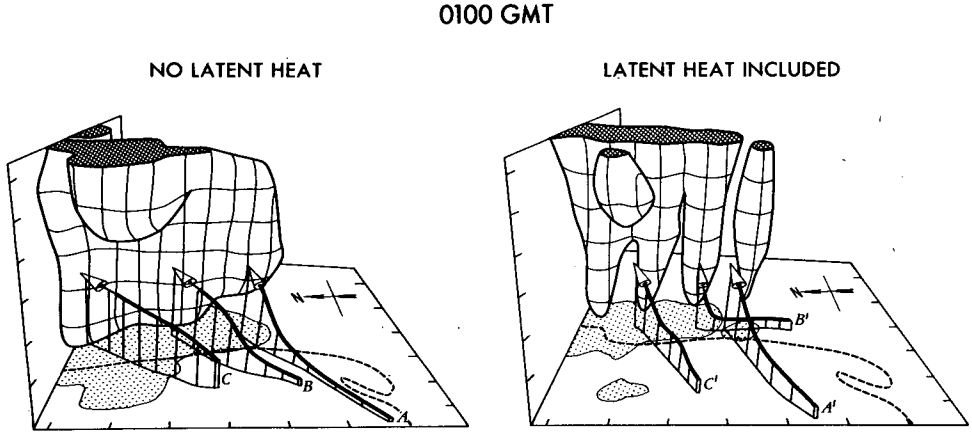

FIG. 17. Comparison of three-dimensional cloud fields and parcel trajectories at 0100 UTC between cases without and with latent heat. Dashed contours indicate horizontal position of 9 g kg^{-1} contour at 887 m. Stippled region on surface indicates that cloudwater is located above it within the field shown. Tick marks in vertical are separated by 1 km. Tick marks in horizontal are in 100-km increments. The arrows on the surface indicate the direction of north.

vergence zone at 0100 UTC, parcel B experienced this lifting 1 h earlier, and parcel C was lifted prior to the 1.75-h time period shown.

In view of the initial dryness of the air advected from west of the dryline, vertical diffusion of moisture upward through the dryline interface must have played a dominant role in moistening this dry air to produce saturation in the case without latent heat release. In fact, such mixing due to turbulence immediately above the dryline is quite realistic; however, the deepening of the cloud is excessive, due in part to this diffusion.

When latent heat release was included, the trajectory analysis indicates that resolved vertical advection was the primary mechanism for supplying this moisture to the cloud system. As the right frame of Fig. 17 shows, parcel B′, the only parcel to terminate within the cloud updraft, was lifted directly from the moist layer below. Parcels A′ and C′, both of which terminated in the clear air between cloud cells, originated in the drier air to the west and had similar paths to their non–latent heat counterparts (although their direction is more eastward). Hence, the buoyancy produced by latent heat release created a positive feedback in this case to increase greatly the supply of low-level moisture to the cloud system.

Figure 18 shows the three-dimensional fields for 0400 UTC when the squall line was developing. In order to emphasize the vertical structure of the trajectory paths, the depth of the fields shown has been reduced to 4.5 km. Up to this height, the cloud structures with and without latent heat are very similar. (Note that comparison between Figs. 9 and 15 at this time showed latent heat to produce a much deeper cloud which is not reflected in the present figure.) The only differences which are evident are: 1) the absence of a shallow cloud connecting the squall line to the north system; and 2) the narrowing of the squall line width in the latent heat case, due to more intense convergence.

In contrast to the earlier time, the effect of latent heat release on parcel trajectories is much less dramatic at 0400 UTC. Parcels A and A′ are seen to have virtually identical paths into the nose of the system, implying negligible influence of diabatic effects on this flow region. The primary change in the paths of the parcels entering the squall line on its flanks is the tendency for trajectories to form sharper angles to the line's axis when latent heat is included. This feature reflects the more intense convergence due to diabatic effects.

Comparison of the trajectory paths for the latent heat case between 0100 and 0400 UTC provides an indication of the differences between the two systems. One can identify similarities in the source regions of parcels B′ and C′ in each case, although the termination points inside each storm system are different. The primary difference lies in the origin of the parcels designated by A′. At 0100 UTC, this parcel, like C′, originated in the dry air to the west; however, at 0400 UTC, because of the rotation of the convergence zone caused by the arrival of the surface front, parcel A′ entered the system from the moist air mass that was now located to the southwest. Because of this, there was now a plentiful supply of moisture into the system at 0400 UTC, not only from the eastern flank of the system, as occurred in the 0100 UTC case, but also from upwind of the nose of the squall line as well.

An important feature of Fig. 18, compared to Fig. 17, is the fact that inclusion of latent heat did not cause the cloud system to break up into cells. In fact, at 0500 UTC, a cell did form on the downwind (northeast) end of the system and moved downstream (see Fig. 14). However, the fact that cell formation in the simulation was suppressed over most of the squall line is an aspect of the simulation that deserves further study. There may be some counterpart to this in radar observations that sometimes show a so-called "solid line" of convection on radar reflectivity displays (Burgess and Curran, 1985). In fact, the 11 April squall line exhibited this solid line structure on operational radar during its early stages of development. Such convection is actually multicellular in character but with the scales of these cells apparently too small to be resolved by the radar; as a result, the broader squall line structure is the only detectable feature. Likewise, in the present model with its 20-km grid size, these small-scale cells

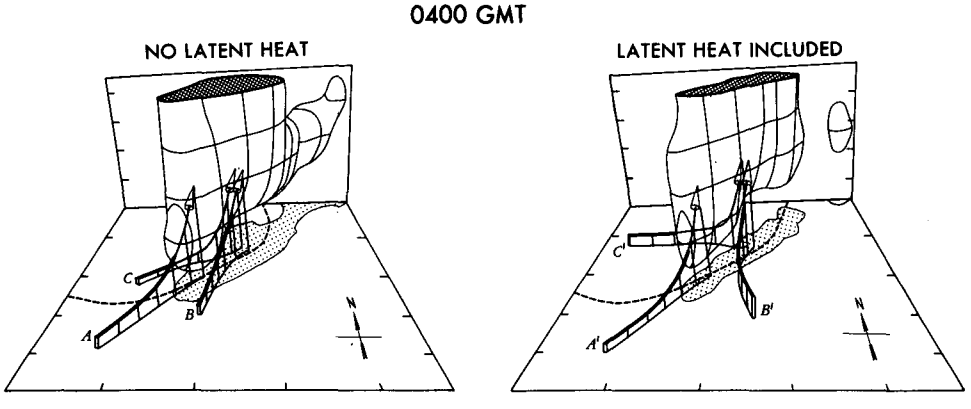

FIG. 18. As in Fig. 17 except at 0400 UTC.

are absent, because they cannot be resolved by the model. One might then speculate that when a meso-beta simulation, such as the present one, produces cellular convection, this might be a region in the real system where convection might produce larger-scale cells.

6. Summary and conclusions

The effects of mesoscale forcing and diabatic heating on the development of a squall line have been investigated by means of a simplified numerical simulation of an observed situation. The meso-beta model used in this study employed data, analyzed from upper air and surface measurements taken at 3 h intervals from the first observing day of the SESAME Experiment, to provide external forcing at the nearby lateral (and surface) boundaries to force the developing mesoscale system. The resulting simulation showed a complex interaction of these different air masses: a moist tongue of southerly air to the east; very warm, dry air blowing from the southwest off the Mexican plateau; and cool air behind a cold front moving into the region from the northwest. Although the simulations were initiated at 1200 UTC 10 April, the primary period of interest for this study was from 2300 UTC 10 April, prior to the squall line formation, to 0600 UTC, when the system was mature.

During the early period prior to 0200 UTC, the cold front was located northwest of the region of interest so that the major external forcing of the mesoscale system in the simulation involved the confluence of the moist air to the east and the warm, dry air to the west. The dryline, which formed the interface between these air masses, was the site of strong low-level convergence in the model as warm air from the southwest moved over this cooler southerly air. This convergence zone, which was forced by these larger-scale processes and thus was not dependent upon moist processes for its existence, was responsible for initiating the resulting convection in the simulation.

As the cold front moved southeastward into the domain, it merged with the dryline, leading to a diffusive breakdown of the dryline's structure at its intersection with the front. As a result, the north–south oriented convergence line associated with the dryline was replaced by the frontal convergence, which had a southwest–northeast orientation. A major effect of this was to rotate the convergence line from an orientation at an angle to the influx of air from the southwest to one in alignment with this airstream. With this new alignment, the upgliding mechanism which was previously responsible for the dryline lifting was replaced by a convergence structure more typical of a surface cold front with cool, dry air behind the front converging with the moist air ahead of it. The warm Mexican airstream from the southwest no longer acted to drive the convergence; in fact, this southwesterly flow now originated in the moist air east of the dryline and provided an influx into the nose of the convergence line of moist air with nearly neutral stratification. This new configuration determined the structure of the developing squall line and seemed to be responsible for the unique plume-like character of the resulting system.

The effect of latent heat on the earlier line system was to enhance the moisture supply to the convective system forming at the western edge of the moist air mass. Without latent heat, the dry air flowing above this air mass was moistened primarily by subgrid-scale vertical diffusion. However, when latent heat was included, the intensified low-level convergence caused by this latent heat release produced direct, resolved lifting of moisture into the system. The convection which developed downstream of the large-scale convergence zone (i.e., the zone which formed independent of latent heating) produced separate, isolated cells which then moved downstream in a manner suggestive of the supercell-type convection that occurred during this period.

The inclusion of latent heat produced less dramatic effects on the squall line but still caused an overall intensification of convection. Its primary effect was to increase and maintain the low-level convergence zone, with a resulting narrowing of the width of the zone and a considerable deepening of cloud penetration through the upper troposphere and into the stratosphere. Also, whereas the convergence zone in the simulation without latent heat achieved a maximum intensity at 0300 UTC and decayed thereafter, the convergence in the latent heat case continued to increase after this time, reaching a peak value of nearly twice that of the non–latent heat case.

A significant feature of the simulation was the failure of the squall line system to break up into convective cells when latent heat was included, as had occurred in the earlier convective system. A primary determinant of this was the alignment of the convergence zone relative to the low-level inflow of moist air. In the earlier case, when the convergence line was more perpendicular to the inflow, air parcels encountered a brief, intense period of lifting that produced cellular structure. In the later squall line case, low-level flow was in alignment with the convergence line; as a result, the air parcels were more gradually lifted over a longer distance. This produced a more reversible process that was less favorable to cell formation in the model.

Finally, in both convective systems, cells tended to develop downstream of the externally imposed convergence zones. It is not possible, in the present study, to determine whether this behavior has a physical basis or is a result of the coarse model resolution, with its correspondingly slower time scales for convective development.

Acknowledgments. The author is very much indebted to Dr. Isidoro Orlanski for his help and support during the course of this research and for his comments regarding the manuscript. I also appreciate the help of Drs. Frank Lipps and Richard Anthes and, particularly, an anonymous reviewer in clarifying and improving

the manuscript. In addition, I would like to thank Professor Dayton Vincent and Mr. Thomas Carney for kindly providing me with the gridded SESAME dataset. The Heavy Precipitation Forecasting Group of the National Meteorological Center provided the precipitation analysis shown in Fig. 16. I also appreciate the graphics support provided by Larry Polinsky and John Baum and the figure preparation provided by John Connor, Phil Tunison, and other members of the GFDL Drafting Group.

REFERENCES

Alberty, R. L., D. W. Burgess, C. E. Hane and J. F. Warner, 1979: *SESAME 1979 Operations Summary.* NOAA/ERL, Boulder, 253 pp.

Anthes, R. A., Y.-H. Kuo, S. G. Benjamin and Y.-F. Li, 1982: The evolution of the mesoscale environment of severe local storms: Preliminary modeling results. *Mon. Wea. Rev.*, **110,** 1187–1213.

——, ——, D. P. Baumhefner, R. M. Errico and T. W. Bettge, 1985: Predictability of mesoscale atmospheric motions. *Advances in Geophysics,* **28B,** 159–202.

Arakawa, A., 1972: Design of the UCLA general circulation model. Numerical Simulation of Weather and Climate. Tech. Rep. 7, Dept. of Meteorology, University of California, Los Angeles, 116 pp.

Barnes, S. L., 1985: SESAME Alphabetical Bibliography. *SESAME Newsletter,* **3**(3), CIMMES/ERL/NOAA, Norman, OK, 8–15.

Benjamin, S. G., 1983: Some effects of surface heating and topography on the regional severe storm environment. Ph.D. dissertation, The Pennsylvania State University, 265 pp.

——, and T. N. Carlson, 1986: Some effects of surface heating and topography on the regional severe storm environment. Part I: 3-D simulations. *Mon. Wea. Rev.*, **114,** 307–329.

Bluestein, H. W., and M. H. Jain, 1985: Formation of mesoscale lines of precipitation: Severe squall lines in Oklahoma during the spring. *J. Atmos. Sci.*, **42,** 1711–1732.

Burgess, D. W., and E. B. Curran, 1985: The relationship of storm type to environment in Oklahoma on 26 April 1984. *Preprints, 14th Conference on Severe Local Storms,* Indianapolis, Amer. Meteor. Soc., 208–211.

Carlson, T. N., R. A. Anthes, M. Schwartz, S. G. Benjamin and D. G. Baldwin, 1980: Analysis and prediction of severe storm environments. *Bull. Amer. Meteor. Soc.*, **61,** 1018–1032.

——, S. G. Benjamin and G. S. Forbes, 1983: Elevated mixed layers in the regional severe storm environment: Conceptual model and case studies. *Mon. Wea. Rev.*, **111,** 1453–1473.

Chang, C. B., D. J. Perkey and C. W. Kreitzberg, 1982: A numerical case study of the effects of latent heating on a developing wave cyclone. *J. Atmos. Sci.*, **39,** 1555–1570.

Danielsen, E. F., 1974: The relationship between severe weather, major dust storms and rapid large-scale cyclogenesis. *Subsynoptic Extratropical Weather Systems,* NCAR PB-247 285, Boulder, 215–241.

Fankhauser, J. C., 1974: The derivation of consistent fields of wind and geopotential height from mesoscale rawinsonde data. *J. Appl. Meteor.*, **13,** 637–646.

Fawcett, E. B., 1977: Current capabilities in prediction at the National Weather Service's National Meteorological Center. *Bull. Amer. Meteor. Soc.*, **58,** 143–149.

Fritsch, J. M., and R. A. Maddox, 1981: Convectively driven mesoscale weather systems aloft. Part II: Numerical simulations. *J. Appl. Meteor.*, **20,** 9–19.

Kalb, M. W., 1985: Results from a limited area mesoscale numerical simulation for 10 April 1979. *Mon. Wea. Rev.*, **113,** 1644–1662.

Koch, S., 1984: The role of an apparent mesoscale frontogenetical circulation in squall line initiation. *Mon. Wea. Rev.*, **112,** 2090–2111.

——, and J. McCarthy, 1982: The evolution of an Oklahoma dryline. Part II: Boundary-layer forcing of mesoconvective systems. *J. Atmos. Sci.*, **39,** 237–257.

Kreitzberg, C. W., 1979: Observing, analyzing, and modeling mesoscale weather phenomena. *Rev. Geophys. Space Phys.*, **17,** 1852–1871.

Kuo, Y.-H., and R. A. Anthes, 1984: Accuracy of diagnostic heat and moisture budgets using SESAME-79 field data as revealed by observing system simulation experiments. *Mon. Wea. Rev.*, **112,** 1465–1481.

McCarthy, J., and S. E. Koch, 1982: The evolution of an Oklahoma dryline. Part I: Meso- and synoptic-scale analysis. *J. Atmos. Sci.*, **39,** 225–236.

Miller, J. E., 1948: On the concept of frontogenesis. *J. Meteor.*, **11,** 169–171.

Moller, A., 1979: The climatology and synoptic meteorology of Southern Plains' tornado outbreaks. Masters Thesis, University of Oklahoma.

——, 1980: Mesoscale surface analysis of the 10 April 1979 tornadoes in Texas and Oklahoma. *Preprints, Eighth Conference on Weather Forecasting and Analysis,* Denver, Amer. Meteor. Soc., 36–43.

Moore, J. T., and H. E. Fuelberg, 1981: A synoptic analysis of the first AVE-SESAME '79 period. *Bull. Amer. Meteor. Soc.*, **62,** 1577–1590.

Ogura, Y., 1975: On the interaction between cumulus clouds and the large-scale environment. *Pure Appl. Geophys.*, **113,** 869–890.

——, and Y.-L. Chen, 1977: A life history of an intense mesoscale convective storm in Oklahoma. *J. Atmos. Sci.*, **34,** 1456–1476.

Orlanski, I., and L. J. Polinsky, 1984: Predictability of mesoscale phenomena. *Mesoscale Observations and Very Short Range Forecasting, Nowcasting II. Proc., Second International Symposium on Nowcasting,* Norrkoping, Sweden, European Space Agency SP-208, Noordwijk, The Netherlands, 271–280.

——, and B. B. Ross, 1984: The evolution of an observed cold front. Part II: Mesoscale Dynamics. *J. Atmos. Sci.*, **41,** 1669–1703.

——, D. Miller and K. Miyakoda, 1984: The impact of initialization analyses in the forecasting of precipitation patterns. *Reprints of Workshop on Very Short-Range Forecasting Systems—Research Aspects,* Boulder, Short- and Medium-Range Prediction Research Publication Series No. 5, World Meteorological Organization, 59–62.

——, B. B. Ross, L. J. Polinsky and R. W. Shaginaw, 1985: Advances in the theory of fronts. *Advances in Geophysics,* **28B,** 223–252.

Ross, B. B., 1986: An overview of numerical weather prediction. *Mesoscale Meteorology and Forecasting,* P. Ray, Ed., Amer. Meteor. Soc., 720–751.

——, and I. Orlanski, 1978: The circulation associated with a cold front. Part II: Moist case. *J. Atmos. Sci.*, **35,** 377–387.

——, and ——, 1982: The evolution of an observed cold front. Part I: Numerical simulation. *J. Atmos. Sci.*, **39,** 296–327.

UCAR, 1984: *The National STORM Program. STORM CENTRAL Phase. Preliminary Program Design.* E. Zipser, Ed., National Center for Atmospheric Research, Boulder, 147 pp.

Vincent D. G., and T. Q. Carney, 1982: Meso-synoptic scale circulation patterns during severe weather outbreaks of 10–11 April 1979. *Preprints, 12th Conference on Severe Local Storms,* San Antonio, Amer. Meteor. Soc., 556–559.

——, ——, J. H. Homan and R. Fulton, 1981: Mesoscale weather patterns during 10–11 April 1979 severe weather outbreak in the southwestern USA. *Proc. from the Joint IAMAP/IAGA Symposium,* Hamburg, European Space Agency ESA-SP-165, Paris, 11–16.